REVIEW ARTICLE

Mueller polarimetric imaging for surgical and diagnostic applications: a review

Ji Qi [1,2,*], *Daniel S. Elson* [1,2,*]

[1] Hamlyn Centre for Robotic Surgery, Institute of Global Health Innovation, Imperial College London, Exhibition Road, London
    SW7 2AZ, UK
[2] Department of Surgery and Cancer, Imperial College London, Exhibition Road, London SW7 2AZ, UK

Polarization is a fundamental property of light and a powerful sensing tool that has been applied to many areas. A Mueller matrix is a complete mathematical description of the polarization characteristics of objects that interact with light, and is known as a transfer function of Stokes vectors which characterise the state of polarization of light. Mueller polarimetric imaging measures Mueller matrices over a field of view and thus allows for visualising the polarization characteristics of the objects. It has emerged as a promising technique in recent years for tissue imaging, improving image contrast and providing a unique perspective to reveal additional information that cannot be resolved by other optical imaging modalities. This review introduces the basis of the Stokes-Mueller formulism, interpretation methods of Mueller matrices into fundamental polarization properties, polarization properties of biological tissues, and considerations in the construction of Mueller polarimetric imaging devices for surgical and diagnostic applications, including primary configurations, optimization procedures, calibration methods as well as the instrument polarization properties of several widely-used biomedical optical devices. The paper also reviews recent progress in Mueller polarimetric endoscopes and fibre Mueller polarimeters, followed by the future outlook in applying the technique to surgery and diagnostics.
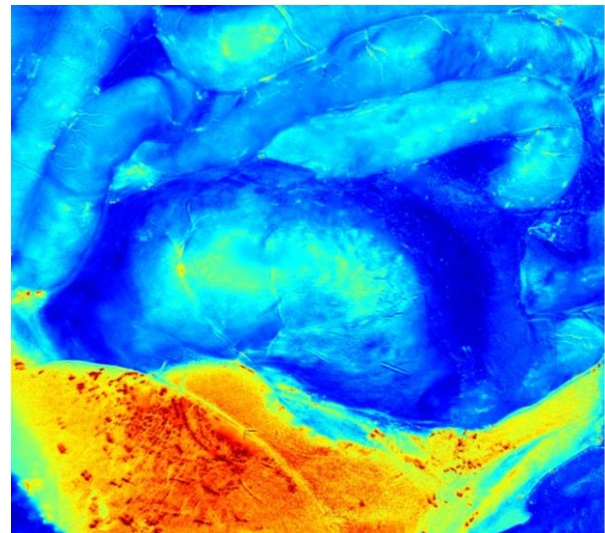
Depolarization image reconstructed from a Mueller polarimetric image of rat abdomen. The liver is at the bottom. The stomach is in the middle. The small bowel is at the top.

1. Introduction

Traditional medical optical techniques for imaging biological tissues only make use of radiant flux and three wavelength bands of light to implement basic colour imaging. State-of-the-art optical imaging has broadened the possibilities considerably and allowed the observation of biological tissue from new perspectives based on additional image contrast mechanisms. Light spectroscopic methods, including point spectroscopy and spectral imaging, utilize wavelength variations from diffuse reflectance, fluorescence or Raman scattering to

* Corresponding author: e-mail ds.elson@imperial.ac.uk, Phone: +44 (0)20 7594 1700, Fax: +44 (0)20 7594 5196
* Corresponding author: e-mail j.qi10@imperial.ac.uk

obtain compositional information of tissue [1]. Interferometric methods take advantage of the coherence and phase of light to analyse scattering related to tissue microstructures [2] and fluid flows [3, 4]. Optical polarization is another fundamental property of light that is able to provide an interesting and unique insight into tissue [5].

Polarization serves as a relatively simple and economical gating tool to separate photons undergoing a small number of scattering events from those which are multiply scattered, and it has been used as a popular add-on option for many biomedical-optical techniques including elastic scattering spectroscopy (ESS), multispectral imaging, conventional white light imaging, fluorescence imaging etc. More specifically, compared with polarization blind ESS, polarized light elastic scattering spectroscopy (PLSS) is able to facilitate scattering spectrum analysis of tissue epithelia – from where the majority of cancers originate – by removing considerable multiply-scattered background signals. PLSS has become as an emerging research field since the late 1990's and numerous biomedical applications have been proposed thereafter. Polarization-gated imaging may enhance image contrast for superficial tissues [6, 7] and deeper vascular structures [8], and confers a limited but cost effective depth resolved imaging ability [9, 10] in comparison with polarization insensitive imaging.

Tissue intrinsic polarization properties, namely tissue depolarization, birefringence and diattenuation also convey morphological, micro-structural and compositional information of tissue with great potential for label free characterization of tissue pathological changes, e.g. nuclear enlargement of cells, collagen remodelling to which conventional polarization blind imaging is not that sensitive [11, 12]. The characteristic polarization information of interest is carried by a 4×4 matrix named a Mueller matrix and this can be experimentally obtained from Mueller polarimetry and polarimetric imaging. In recent years, an increasing number of biomedical applications of Mueller polarimetric imaging techniques have been proposed [5], e.g. oral cancerous legion detection [13], cervical cancer and colon cancer detection and staging [12, 14-19], assessment of cancer therapy [20], partial bladder obstruction diagnosis [21], guiding mass spectrometry for instant pathology [22], characterizing collagen fibres [23], and these have demonstrated advantages over polarization blind imaging .

Mueller polarimetric imaging is however, mainly based on bulky free-space optics with many systems operated in transmission geometry. It often involves time sequential acquisition of a number of radiometric images which makes real time implementation challenging. The fusion of the polarimetric imaging technique and optical instruments like medical endoscopes for real time surgical guidance and optical diagnostic applications would require proper miniaturization, which is one of the challenges to translate the technique from an optical laboratory to the clinic. The acquisition time of polarimetric images still needs to be shortened for real time applications. Clinical interpretation of polarimetric images remains another challenge. Such interpretation would have to be based on a considerable investigation of the correlation of the polarimetric image contrast and its histological origins, which may involve physical interpretation of polarimetric data, modelling and simulation of polarized light propagation in complex-structured anisotropic tissues, microscopy and tissue pathological studies, as well as systematic clinical trials and statistical measures of the performance of polarimetric imaging.

Thanks to the compelling potential of polarimetric imaging, some of these challenges have been addressed in recent studies. This review introduces the basis of the Stokes-Mueller formulism, polarization properties of biological tissues and considerations in the construction of Mueller polarimetric imaging devices for surgical and diagnostic applications including primary configurations, optimization procedures and calibration methods. The instrumental polarization properties of several widely-used biomedical optical components and instruments represented by traditional rigid endoscopes, GRIN lenses and single mode fibres, are outlined in this review. Advances in interpretation methods of the comparatively implicit 4×4 Mueller matrix over the past decades have enabled physically meaningful polarization properties - that is, depolarization, retardance and diattenuation - to be recovered from highly depolarizing turbid media like biological tissues. This has facilitated investigation of the correlation between those physically meaningful polarization properties with the medically meaningful pathological origins. Several interpretation methods are briefly introduced in this review. An increasing number of biomedical applications of Mueller polarimetric imaging techniques have been proposed, and this has paved the way for translational and preclinical trials. Progress made on the integration of medical endoscopes and single mode fibres with Mueller polarimetric ability has been detailed, followed by a summary of recent progress and the future outlook for surgical and diagnostic applications of these techniques.

2. Stokes parameters and Mueller matrices

Polarization characterizes the oscillation states of the electric (or magnetic) field of a light wave. The disturbance of a plane time-harmonic transverse field may either be along a single direction or may rotate periodically at the wave frequency, known respectively as the linear polarization and circular/elliptical polarization states. The disturbance may also be along a random direction in the temporal and spatial domains, which is known as unpolarized (fully random) or partially polarized (partially random) light. The above description

of polarization is based on classical electrodynamics. It should be mentioned that the concept of polarization may also be applied to individual photons which are either right or left circularly polarized determined by the spin angular momentum of the photon according to quantum mechanics [24]. The classical description is normally sufficient for tissue polarimetry measurements.

The term "polarization" may conventionally refer to the state of polarization (SOP) of a coherent wave, an overall temporal and spatial average SOP for incoherent waves, or polarization properties characterizing the transformation of SOPs. The oscillation state of the electric field vector E of light waves is conventionally used to represent SOPs. The solution of Fresnel's wave equations for a plane time-harmonic light wave propagating along the z axis in a Cartesian coordinate system x-y-z in terms of the electric field are

$$J = \begin{bmatrix} E_x \\ E_y \end{bmatrix} = \begin{bmatrix} E_{0x}e^{i(\omega t - kz + \delta_x)} \\ E_{0y}e^{i(\omega t - kz + \delta_y)} \end{bmatrix} \propto \begin{bmatrix} E_{0x}e^{i\delta_x} \\ E_{0y}e^{i\delta_y} \end{bmatrix} \tag{1}$$

where E_{0x}, E_{0y}, ω, k, δ_x and δ_y stand for the amplitudes along the x and y axis, the angular frequency, the wave number and the phases of the two orthogonal electric fields along the x and y axis respectively. The direction of the x axis is perpendicular to the z axis but otherwise arbitrary, and is also sometimes expressed as "horizontal" in the following discussion ("horizontal" in quotation marks means it may not be necessarily the same as the horizontal direction in the world coordinate system). By factoring out the time-space propagator (ωt-kz), Equation (1) can be expressed in the form of a two-element vector $[E_x, E_y]$ that is widely used to characterize polarized light, called a Jones vector. A Jones matrix is accordingly defined to be a 2×2 complex matrix that represents a transfer function of Jones vectors. The Jones formulism is preferred when studying phenomena involving coherent superposition e.g. interference. Jones vectors are unable to characterize a statistically averaged SOP per unit area/time of light, namely, fully polarized light, partially polarized light and unpolarized light, resulting from the stochastic nature of partially coherent and incoherent waves. The overwhelming majority of light sensors are based on radiometry which measures the spatial and temporal average of optical energy flux density (characterized by the Poynting vector) of a light wave per unit time referred to as irradiance or intensity with the unit Watt/m^2, which makes it difficult to explicitly determine Jones vectors defined in the amplitude and phase domain of the electric field.

Four parameters developed by George Gabriel Stokes can address the problems above. The parameters are determined by a set of radiometric intensity measurements using "horizontal" (I_H), "vertical" (I_V), +45° (I_{45}), -45° (I_{-45}) linear, as well as left (I_L) and right (I_R) circular polarization analysers. The parameters are conventionally written as a four-element vector named the Stokes vector S, written as

$$S = \begin{bmatrix} S_0 \\ S_1 \\ S_2 \\ S_3 \end{bmatrix} = \begin{bmatrix} I_H + I_V \\ I_H - I_V \\ I_{45} - I_{-45} \\ I_L - I_R \end{bmatrix} \tag{2}$$

The degree of polarization (DOP) of light refers to the (averaged) intensity of the polarized portion of the light beam out of the (averaged) total intensity. It can be easily interpreted from a Stokes vector

$$DOP = \frac{\sqrt{S_1^2 + S_2^2 + S_3^2}}{S_0} \tag{3}$$

The DOP is 1 for fully polarized light, 0 for unpolarized light, and in the range 0-1 for partially polarized light. The DOP can never be more than 1 for a physically realizable Stokes vector [25]. Similarly, degree of linear polarization (DOLP) and degree of circular polarization (DOCP) of light are the (averaged) intensity of the linearly polarized and circularly polarized portion of the light beam out of the (averaged) total intensity respectively,

$$DOLP = \frac{\sqrt{S_1^2 + S_2^2}}{S_0} \tag{4}$$
$$DOCP = \frac{S_3}{S_0}$$

One of the advantages of using Stokes parameters is that they are explicitly determined by several radiometric intensity measurements rather than from the complex electric field that is difficult to measure. Another advantage is that Stokes parameters are able to characterize statistically averaged SOPs of light per unit area/time, namely, fully polarized light, partially polarized light and unpolarized light. Stokes parameters are able to characterize all the SOPs. Additional care should be taken in practice when they are used with coherent light sources that may result in speckles [10, 26-28]. For example, the size of the detector used for Stokes polarimetry should normally be large enough to cover a sufficient number of speckles, that is, the detection area should be much larger than a typical speckle size, in order to determine the depolarization property of a turbid media [26, 29].

To graphically display a SOP of light, a Euclidean space constructed by three standard orthogonal bases corresponding to the last three elements of a Stokes vector S_1-S_2-S_3 (referred to as Poincare domain in this review) is widely used, as shown in Figure 1. In this domain, a SOP is represented by a vector determined by [S_1/S_0, S_2/S_0, S_3/S_0], and the DOP of light is therefore the length of this vector. All of the possible SOPs of fully polarized light constitute a sphere with a radius 1 - named the Poincare sphere by convention - while vectors for partially polarized light are distributed within the sphere.
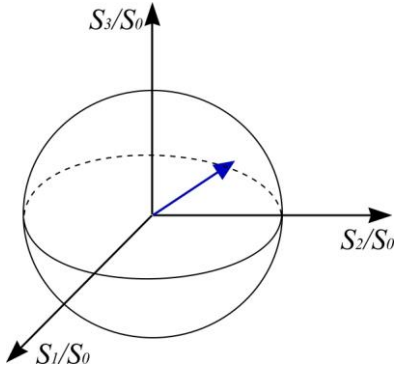
Figure 1. The Poincare sphere is defined in a Euclidean space constructed by three standard orthogonal bases corresponding to the last three elements of a Stokes vector S_1-S_2-S_3 (referred to as Poincare domain in this review). The blue vector represents a SOP of light, which represented by a vector determined by [S_1/S_0, S_2/S_0, S_3/S_0]. All of the possible SOPs of fully polarized light constitute a sphere with a radius 1 - named the Poincare sphere - while vectors for partially polarized light are distributed within the sphere.

The SOP of light may be transformed during polarized light-matter interactions, and such a transformation reflects the polarization properties of matter. The mathematical description of the Stokes vector transformation is a 4×4 matrix named a Mueller matrix, which was devised by Hans Mueller in 1947 [30]. If the SOP of the incident light is characterized by the input Stokes vector S_{in}, the polarization properties of the matter is described by the Mueller matrix M, and the SOP of emergent light is represented by the output Stokes vector S_{out}, then the process of the interaction is given by the following set of linear equations,

$$S_{out} = MS_{in} = \begin{bmatrix} m_{11} & m_{12} & m_{13} & m_{14} \\ m_{21} & m_{22} & m_{23} & m_{24} \\ m_{31} & m_{32} & m_{33} & m_{34} \\ m_{41} & m_{42} & m_{43} & m_{44} \end{bmatrix} S_{in} \qquad (5)$$

Mueller matrices are a transfer function of Stokes vectors, and are defined in Stokes vector space, so they inherit the advantages of Stokes vectors. Since Stokes vectors are explicitly measurable and are able to describe partially polarized light, a Mueller matrix can be relatively easily determined experimentally and also contains depolarization information, which is of great value for highly scattering media with strong depolarization like biological tissues.

3. Fundamental polarization properties

There are in essence three fundamental polarization properties of matter, namely, depolarization, diattenuation

and retardance [31]. Diattenuation refers to the phenomenon that the transmittance (or reflectance) of matter depends on the SOP of incident light. Dichroism is a synonym to diattenuation and is usually used to characterize the diattenuation properties of materials. The magnitude of diattenuation D is a scalar defined by a maximum and a minimum transmittance (or reflectance) represented by T_{max} and T_{min} as

$$D \equiv \frac{T_{max} - T_{min}}{T_{max} + T_{min}} \qquad (6)$$

T_{max} and T_{min} can be readily obtained from the first row of the Mueller matrix based on the definition of transmittance (or reflectance) and the Mueller calculus [25],

$$T_{max} = m_{11} + \sqrt{m_{12}^2 + m_{13}^2 + m_{14}^2}$$
$$T_{min} = m_{11} - \sqrt{m_{12}^2 + m_{13}^2 + m_{14}^2} \qquad (7)$$

The diattenuation vector D is defined as [32]

$$D = \frac{1}{m_{11}} [m_{12} \quad m_{13} \quad m_{14}]^T \qquad (8)$$

m_{12} and m_{13} refer to "horizontal" and 45° linear diattenuation parameters, and contribute to the total linear diattenuation value. m_{14} represents circular diattenuation. Thus, the magnitude of diattenuation D is the length of the diattenuation vector D and ranges from 0 (representing no diattenuation) to 1 (representing full diattenuation),

$$D = \|D\| = \frac{\sqrt{m_{12}^2 + m_{13}^2 + m_{14}^2}}{m_{11}} \qquad (9)$$

A canonical form of the diattenuation matrix M_D can be constructed based on the diattenuation vector D [31],

$$M_D = \begin{bmatrix} 1 & D^T \\ D & m_D \end{bmatrix}$$
$$m_D = aI_{(3)} + b(DD^T) \qquad (10)$$
$$\begin{cases} a = \sqrt{1 - |D|^2} \\ b = \frac{1 - \sqrt{1 - |D|^2}}{|D|^2} \end{cases}$$

where $I_{(3)}$ stands for a 3×3 identity matrix. Matter may demonstrate no diattenuation with M_D an identity matrix (the magnitude of diattenuation D is equal to 0), partial diattenuation as one of its polarization properties, or pure diattenuation as its sole polarization property (the magnitude of diattenuation D is equal to 1). Diattenuators are those elements that show pure diattenuation only. When the magnitude of linear diattenuation of such an element is close to 1, it is referred to as a linear diattenuator, also conventionally called a linear polarizer.

In comparison to diattenuation that is mainly in the amplitude domain, retardance is a polarization dependent process in the phase domain of light. Retardance refers to

the phenomenon of phase difference between two orthogonally polarized components of light when propagating through some medium. Retardance characterizes a rotation transformation in the Poincare domain. Therefore, retardance is represented by the following Mueller matrix[31],

$$M_R = \begin{bmatrix} 1 & 0 \\ 0 & m_R \end{bmatrix} \quad (11)$$

in which m_R is a 3D rotation matrix. The magnitude of retardance is the effective rotation angle in radians determined from the rotation matrix by

$$R = \cos^{-1}\left(\frac{\mathrm{Tr}(M_R)}{2} - 1\right) \quad (12)$$

Retardance can be further broken down into linear retardance and circular retardance [31]. Linear retardance may stem from reflection, refraction, scattering, birefringent materials and form-birefringence effects. Birefringence is a conventional term to characterize such optical properties of materials with varying refractive indices (real part) for linearly polarized light with different polarization direction. Linear retardance can be outlined by two parameters: a linear phase retardance value δ_L in radians, and an anisotropy axis (e.g. fast axis of a waveplate) orientation angle φ, both of which are often used to reconstruct retardance images in polarimetric imaging. Linear retardance contains three consecutive rotations in the Poincare domain: a rotation of 2φ in the S_1-S_2 plane, a rotation of δ_L in the S_2-S_3 plane and a rotation of -2φ in the S_1-S_2 plane. A linear retardance matrix can thereby be written as

$$M_{LR} = \begin{bmatrix} 1 & 0 \\ 0 & m_{LR} \end{bmatrix} \quad (13)$$

$$m_{LR} = \begin{bmatrix} \cos 2\varphi & -\sin 2\varphi & 0 \\ \sin 2\varphi & \cos 2\varphi & 0 \\ 0 & 0 & 1 \end{bmatrix}\begin{bmatrix} 1 & 0 & 0 \\ 0 & \cos\delta_L & \sin\delta_L \\ 0 & -\sin\delta_L & \cos\delta_L \end{bmatrix}\begin{bmatrix} \cos 2\varphi & \sin 2\varphi & 0 \\ -\sin 2\varphi & \cos 2\varphi & 0 \\ 0 & 0 & 1 \end{bmatrix}$$

A physical element with only homogeneous linear retardance is a waveplate, also known as a linear retarder. Circular retardance, also known as optical rotation, optical activity and circular birefringence originates from the different (real part of) refractive indices for left and right circularly polarized light. Circular retardance geometrically represents a rotation of δ_C along S_1-S_2 plane. Its Mueller matrix only depends on the circular phase retardance value δ_C and is specified by

$$M_{CR} = \begin{bmatrix} 1 & 0 \\ 0 & m_{CR} \end{bmatrix}$$

$$m_{CR} = \begin{bmatrix} \cos\delta_c & \sin\delta_c & 0 \\ -\sin\delta_c & \cos\delta_c & 0 \\ 0 & 0 & 1 \end{bmatrix} \quad (14)$$

A general retardance matrix M_R is normally regarded as a product of linear retardance matrix and circular retardance matrix,

$$M_R = M_{LR}M_{CR} = \begin{bmatrix} 1 & 0 \\ 0 & m_{LR} \end{bmatrix}\begin{bmatrix} 1 & 0 \\ 0 & m_{CR} \end{bmatrix} \quad (15)$$

Thus linear phase retardance value and circular phase retardance value can be readily calculated from the retardance matrix that is normally given in a Mueller matrix decomposition procedure. One of the ways to yield these values is

$$\delta_L = \cos^{-1}\left(\sqrt{[M_R(2,2)+M_R(3,3)]^2 + [M_R(3,2)-M_R(2,3)]^2} - 1\right)$$

$$\delta_C = \tan^{-1}\frac{M_R(3,2)-M_R(2,3)}{M_R(2,2)+M_R(3,3)} \quad (16)$$

The third property, depolarization refers to a process of loss in coherency of phase or amplitude of an electric field, manifesting a reduction of DOP of the incident light. Physically, depolarization originates from the average effects of rapidly temporally, spatially and/or spectrally varying retardance and diattenuation [25], which are normally related to disordered media like turbid media and rough surfaces, as well as broadband light sources. The Mueller matrix of a depolarizing medium is normally diagonal, written as [31],

$$M_\Delta = \begin{bmatrix} 1 & 0 & 0 & 0 \\ 0 & \Delta_2 & 0 & 0 \\ 0 & 0 & \Delta_3 & 0 \\ 0 & 0 & 0 & \Delta_4 \end{bmatrix} \quad 0 \le |\Delta_2|,|\Delta_3|,|\Delta_4| \le 1 \quad (17)$$

Δ_2, Δ_3 and Δ_4 denote the principal polarization maintaining powers along three principal axes in the Poincare domain. The depolarization power is accordingly defined in a complementary way as $1-|\Delta_2|$, $1-|\Delta_3|$ and $1-|\Delta_4|$ [31]. In the product decomposition method for Mueller matrices represented by Lu-Chipman's polar decomposition method, a more general form of a depolarization matrix (without considering polarizance) can be written as

$$M_\Delta = \begin{bmatrix} 1 & 0 \\ 0 & m_\Delta \end{bmatrix} \quad (18)$$

in which m_Δ represents the bottom right 3×3 elements of M_Δ and is a symmetric matrix. The eigenvalues of m_Δ reveal the principal polarization maintaining powers.

Beside the depolarization power there are a number of other parameters to characterize depolarization including depolarization index and average degree of polarization [33, 34]. These two parameters can be obtained from Mueller matrices directly rather than through a decomposition procedure. The depolarization index (DI) was first proposed by Gil *et al.* according to a geometric scheme of depolarization in "configuration space", which is a 16 dimensional vectorized Mueller matrix hyperspace where the axes/basis correspond to the 16 elements of the Mueller matrix [34]. All the non-depolarizing Mueller matrices are distributed on a hyper-spherical surface in

this hyperspace. All the depolarizing matrices are inside the hyper-sphere. DI is expressed as

$$DI = 1 - \frac{\sqrt{tr(MM^T) - m_{11}^2}}{\sqrt{3}m_{11}} \qquad (19)$$

The numerator of the second term is the distance from an ideal depolarizer to the interpreted Mueller matrix in the hyperspace. The denominator is the radius of the hyperspherical surface of non-depolarizing Mueller matrices. DI is 1 for an ideal depolarizer and 0 for non-depolarizing matrices. The average degree of polarization is defined based on the DOP of the emergent light from a sample. As shown in Equation (5) and (3), the DOP of the emergent light can be considered as a function of the incident polarization state (represented by its Stokes vector S_{in}), and is determined by the product of the Mueller matrix of the sample and S_{in}. The average degree of polarization is thus obtained from the arithmetic mean of the DOP of emergent light corresponding to all of the possible SOPs of fully polarized incident light.[33]. These depolarization parameters are useful tools to study depolarization [35-37] especially when it is not necessary to further invert the Mueller matrix for retardance and diattenuation information.

4. Polarized light and biological tissue

As a result of refractive index non-uniformity at a micro-scale arising from, for example, extracellular proteins like collagen fibrils, cell membranes, cytoplasms, nuclei, organelles etc. [11, 38-40], elastic scattering is a major optical interaction between polarized light and biological tissue. Besides scattering, there are a range of absorbers in tissue including oxygenated and deoxygenated haemoglobin, melanin, water, adipose tissue and fat [41, 42]. Hence, biological tissues are recognised as highly scattering media with considerable optical absorption.

The polarization analysis during a single scattering event in tissue can be conducted through a number of scattering theories [43-45]. Among them, Mie scattering theory for spherical scatterers is widely employed for tissue scattering analysis [11, 46, 47], which for a single scattering event manifests a Mueller matrix in the form of a diattenuated retarder, represented by M_{DR} [43]

$$M_{DR} = \begin{bmatrix} a & b & 0 & 0 \\ b & a & 0 & 0 \\ 0 & 0 & c & -d \\ 0 & 0 & d & c \end{bmatrix}$$

$$a = \frac{1}{2}(|P_2|^2 + |P_1|^2), \quad b = \frac{1}{2}(|P_2|^2 - |P_1|^2) \qquad (20)$$

$$c = \frac{1}{2}(P_2^* P_1 + P_2 P_1^*), \quad d = \frac{i}{2}(P_2^* P_1 - P_2 P_1^*)$$

where * denotes the complex conjugate, and P_1 and P_2 are complex functions of scattering angles, refractive indices of the particle and medium and size parameters of particles (diameter/wavelength), which can be directly determined from Mie scattering theory. An individual scattering event is not a depolarization process for a chosen scattering plane and does not lead to loss of total DOP of light, although there might be conversion between DOLP and DOCP due to scattering-induced retardance and diattenuation. (Nevertheless, as is the case for experimental situations with a finite small numerical aperture and a finite far field, averaging over scattering planes leads to depolarization.) The linear diattenuation and linear retardance stemming from a single scattering event is a function of the scattering angle as well as the refractive index and size parameter of the scatterer. Diattenuation and retardance is usually more pronounced for spherically asymmetric particles. Note that although Mie scattering theory can be used for a sphere of any size, when the size of the scatterer goes down to a dimension much smaller than the wavelength, the Rayleigh approximation of Mie theory or Rayleigh scattering theory can be applied for convenience. The particles that meet the Rayleigh limit are called Rayleigh scatterers, and those for which the size is comparable or larger than wavelength are called Mie scatterers by convention in this review. The element d in Equation (20) becomes zero for Rayleigh scatterers, and its Mueller matrix thus reduces to a diattenuation matrix without retardance.

$$M_D = \begin{bmatrix} \cos^2(\theta)+1 & \cos^2(\theta)-1 & 0 & 0 \\ \cos^2(\theta)-1 & \cos^2(\theta)+1 & 0 & 0 \\ 0 & 0 & 2\cos(\theta) & 0 \\ 0 & 0 & 0 & 2\cos(\theta) \end{bmatrix} \qquad (21)$$

Before leaving tissue of considerable optical thickness, light may undergo multiple scattering, which randomizes not only the direction of light propagation but also the polarization state, resulting in depolarization and normally the reduction of both DOLP and DOCP. The depolarization power of tissue is normally defined as one minus the "polarization maintaining power". The polarization maintaining power essentially refers to the ratio between non-depolarized emergent light intensity and the total emergent light intensity. Notice that the information in a depolarization power image is completely equivalent to a polarization maintaining power image.

Contributions to the non-depolarized emergent light include those photons undergoing a single or a limited number of scattering events, mainly conveying information about a superficial tissue volume within which light is not multiply scattered. Hence, the depolarization power image (or polarization maintaining power) can be used to enhance the contrast for the superficial non-depolarized tissue region, corresponding to the epithelium from which a great number of diseases and cancers originate [48]. Contributions to the

depolarized portion of the emergent light include photons undergoing multiple scattering, which have longer average pathlengths and mainly convey the information from deeper tissue. The mechanism explained above is known as polarization gating and is normally used to distinguish light undergoing a small number of scattering events from that which is multiply scattered. Demos *et al.* reported that such a mechanism could be used to enhance the image contrast for both tissue surface and subsurface [49, 50]. Jacques *et al.* used polarization gating to reveal the disruption of the normal texture of the papillary and upper reticular dermis in human skin [6, 7]. As a highly cost effective solution to raise the image contrast, depolarization techniques have been applied to minimally invasive surgery [51-53] and optical diagnostics [54, 55]. In most of these studies, depolarization power (or polarization maintaining power) images were estimated from passive polarization detection by recording images using co-polarization and cross-polarization with respect to the illumination polarization. The difference between co-polarization and cross-polarization images was used to represent the polarization maintaining power image. The cross-polarization image itself is used to characterise the fully depolarised multiple scattering image with information about deeper tissue.

In non-imaging spectroscopy techniques such as elastic scattering spectroscopy (ESS), polarization may be used to decouple single-scattering spectra from multiple-scattering ones. A great number of diseases like most cancers originate from the epithelium that is located in the regime of single-scattering. Modelling single-scattering to quantify the information of interest about scatterers is far less challenging and requires less computation than with modelling multiple-scattering that involves a series of stochastic processes. Perelman *et al.* developed a scattering spectroscopy technique to identify the light component that is singly scattered by near-surface epithelial cell nuclei [56], since the near-backward scattering light from the cells is dominated by cell nuclei [56-58]. Perelman used a model based method to select single-scattering spectra from the multiple-scattering spectra. The technique was significantly improved by introducing polarization gating to extract single-scattering spectra from multiple-scattering ones, proposed by Backman *et al.* in 1999 [11]. Polarized light scattering spectroscopy incorporating Mie scattering analysis allowed interrogation of the epithelial cell nuclear size distributions from the diffuse background [11, 59, 60]. The first PLSS system was constructed in free space with approximately collimated light and well-defined scattering angles approximating to 180°, so that Mie theory could be easily used to study the scattering spectrum [11]. The system was further improved by using a Fourier lens and a scanning slit spectrometer in order to obtain the wavelength-resolved spectrum and the angle-resolved spectrum at the same time [61, 62]. PLSS fibre optic probes were then developed by Sokolov *et al.* [63] and Mourant *et al.* [64], and were used for characterising

mammalian cells [64] and detecting local tissue changes in the oral cavity [65]. More advanced fibre optic probes for PLSS made use of gradient-index (GRIN) lens to implement depth selective measurement from a range of near surface depths (100-200 μm) to interrogate blood supply [66, 67]. A great number of translational studies for diagnosis of breast cancer [68], prostate cancer[69], intraoperative determination of sentinel lymph node status in the breast [70], colonic lesions [71], oral premalignancy [72], high grade dysplasia and cancer in Barrett's oesophagus [73, 74], cervix neoplasia [75, 76], investigation of the nature of aceto-whitening in cervix cancer inspection [77-82], gold nanoparticle sizing [83], and monitoring apoptosis in cell cultures [84-86] have demonstrated that LSS provides a promising solution for cell culture monitoring, tissue surveillance and biopsy guidance in a relatively simple and cost effective configuration.

It is noted that in many of these applications of polarization gating techniques it is assumed for simplicity that the tissue is isotropic with negligible diattenuation and retardance, therefore only linear depolarization images/spectra need to be obtained by measuring co-polarized and cross-polarized images/spectra with respect to incidence polarization. However, these approximate depolarization signals may be dependent on the angle between incidence polarization and invisible principal axes (e.g. fast axis in linear retardance) of anisotropic tissues. This invisible angle is difficult to control in practice, and would result in potential irreproducibility during measurements and lead to errors in image/spectrum analysis.

Mueller polarimetry can be applied to anisotropic tissues, since linear and circular depolarization as well as other polarization parameters of interest can be achieved independent of tissue anisotropy using proper interpretation methods of Mueller matrices (which will be introduced in Section 5). The mechanisms for depolarization of linearly and circularly polarized light are not exactly the same. Without consideration of absorption, DOLP reduces during multiple scattering processes since the reference frames (scattering planes for one scattering event) are significantly scrambled in a series of consecutive scattering events occurring in three dimensional space [87]. That is, linear depolarization arises from the non-coplanar trajectories of light rays in scattering media. The possibility of non-coplanarity increases as the number of scattering events rises [87]. Circular depolarization is caused by the propagation direction of circularly polarized light and the randomization of its helicity [88]. It has been found that in a suspension of spherical scatterers linear depolarization is lower than circular depolarization for small spheres (Rayleigh scatterers), and also for large spheres with relative refractive index close to 1 (following Rayleigh-Gans approximation or the first Born approximation, known as optically "soft" or "tenuous" [43]), whereas the reverse is true for large spheres with

relative refractive index much larger than 1 (Mie scatterers) [14, 87-92]. It was also reported that linearly polarized light is better preserved through longer propagation distances than circularly polarized light in most biological tissues including fat, tendon, artery, myocardium, colon, bladder [14, 16, 17, 20, 93-95] due to the significant contribution from relatively low refractive index large scatterers like cell nuclei and presence of Rayleigh scatterers including various cell organelles and other biological particles [14, 96]. A known exception with linear depolarization larger than circular depolarization is blood, since red blood cells are anuclear and do not have abundant organelles [93]. Overall, the comparison of tissue linear and circular depolarization can provide interesting information about scatterers (e.g. scatterer sizes) which might produce more applications in the future [89, 97]. Different depolarization mechanisms for linearly and circularly polarized light also result in the non-depolarized backscattered linearly and circularly polarized light probing different tissue volumes, allowing depth resolved imaging of isotropic tissue by adjusting the ellipticity of the incident polarization [9, 98].

Besides scattering, tissue absorption also has a significant influence on depolarization. In general, multiply scattered photons are more likely to be absorbed due to longer propagation pathlengths. As a result, absorption reduces average propagation pathlengths or average number of scattering events, leading to a weaker depolarization effect [94, 99, 100]. The absorption may therefore actually cause interference with scattering analysis based on depolarization spectra, which deserves more attention and effort to correct. An individual molecule with anisotropic structures, like amino acids, may manifest polarization dependent absorption (diattenuation) [101], but absorption by bulk tissue does not exhibit polarization dependence in most cases as a result of the random spatial distribution of the molecules in tissue.

The scattering induced retardance from spherical and randomly oriented non-spherical scatterers in tissue is normally weak in the multiple-scattering regime. The observable tissue retardance mainly originates from anisotropic fibrous tissue structures like collagen fibrils and elastin fibres, which are equivalent to uniaxial birefringent crystals [101-103]. Cancerous tissue is typically associated with changes in collagen components, e.g. deposition of collagen fibrils resulting from an increased number of fibroblasts [104]. Detecting these structural proteins - particularly the content and organizations of collagen - is of significance because it is one of the most fundamental components in tissue and can be used as a marker for cancer [104, 105]. Besides cancer detection, retardance is also applied to the investigation of collagen rich tissues and related diseases like partial bladder outlet obstruction [21, 106], osteoarthritis and other cartilage diseases [107], or determining 3D direction of collagen fibres in knees [23] and retina (often imaged by polarization sensitive OCT) [108-110].

There may also be a contribution to circular tissue retardance from asymmetric chiral molecules like glucose. Accurate monitoring of blood glucose levels non-invasively is a long-standing challenge and a solution is strongly desired for diabetic patient management and to prevent complications. Circular retardance is proportional to the concentration of glucose, and therefore transdermal measurement of circular retardance would provide a potential solution. It has been demonstrated that the glucose concentration could be detected non-invasively from a turbid medium experimentally in transmission [111-113] and in simulation for reflection using a polarization sensitive Monte Carlo method [113]. The actual physiological concentration of glucose in blood is extremely low (4.4 to 6.1 mMol/L), even in hyperglycaemia (up to 10 mMol/L) [114], and additionally optical rotation induced by glucose is as small as $0.00095°cm^{-1}(mMol/L)^{-1}$[115]. Therefore a polarimeter with extremely high accuracy would be required, particularly in reflection mode, and other tissue polarization properties may still influence the optical rotation and interfere with detection.

Tissue diattenuation is normally less pronounced than depolarization and retardance for bulk tissues, although this may not fully apply to polarization sensitive OCT that provides tomographic information, but this is not in the scope of this review.

5. Interpretation of Mueller matrix into fundamental polarization properties

Polarized light-tissue interactions convey rich tissue information, and Mueller matrices provide the foundation for a comprehensive assessment of tissue in terms of polarization. Retardance and diattenuation strongly entangle with depolarization as a result of the strong scattering nature of biological tissues. Moreover, in practice, the measured Mueller matrix is also dependent to the azimuthal orientation between the invisible anisotropic axis of tissue and the defined "horizontal" axis of a Mueller matrix which is difficult to control in practice and may lead to variations during inter/intra sample measurements. It is therefore important to interpret Mueller matrices in terms of fundamental polarization properties with an intuitive physical explanation so as to 1) facilitate investigation and understanding of biophysical origin of the polarimetric signals, and 2) obtain azimuthal orientation angle independent parameters to maintain the reproducibility of results.

Remarkable advances have been made to interpret Mueller matrices in terms of these fundamental polarization properties. A number of methods including Lu-Chipman's polar decomposition [31], reverse polar decomposition [116], symmetric decomposition [117], differential decomposition [118-123] and root

decomposition [37, 124], Mueller matrix transformation techniques [125-131], Cloude's sum decomposition [132], serial parallel decomposition [133], etc. have been developed. Interpretation of Mueller matrices is still a very active research field so more advances can be expected. Here we present a very brief review of some methods that have been successfully translated to the study of tissue.

5.1 Factor product decomposition

One of the earliest proposed and most widely adopted methods is Lu-Chipman's polar decomposition, in which a Mueller matrix is decomposed into a three-factor product of a depolarization matrix, a retardance matrix and a diattenuation matrix in sequence, expressed by

$$M = M_{\Delta(LC)} M_{R(LC)} M_{D(LC)} \tag{22}$$

It is noted that $M_{\Delta(LC)}$ here is a modified depolarization matrix containing polarizance parameters in its first column. Lu-Chipman's decomposition has been validated with well-controlled turbid media which turned out to yield reliable measures of the fundamental polarization properties [113, 134, 135], and is thus a popular interpretation method applied in a considerable number of tissue polarimetry studies [12, 13, 18-20, 136, 137].

The idea behind Lu-Chipman decomposition is to find an equivalent cascade of a diattenuator, a retarder, and a depolarizer that has the same effective Mueller matrix to the recorded Mueller matrix. There may exist other equivalent cascades derived from other product based decomposition methods. In the reverse decomposition method which is also a three-factor product decomposition derived from Lu-Chipman's polar decomposition method, a Mueller matrix is modelled as a cascade of a depolarizer, a diattenuator and a retarder that is exactly in reverse order with respect to Lu-Chipman's polar decomposition model. The interpreted Mueller matrix can then be decomposed into

$$M = M_{D(rev)} M_{R(rev)} M_{\Delta(rev)} \tag{23}$$

$M_{\Delta(rev)}$ here is also a modified depolarization matrix containing diattenuation parameters in its first row. It is noted that the order and the number of the equivalent elements in the decomposition models do have an influence in the interpreted depolarization, retardance and diattenuation properties [138]. Comparison studies of Lu-Chipman and reverse decomposition showed that these two methods yield consistent decomposition results providing that the magnitude of diattenuation of the medium is low [139]. The same study further confirmed that diattenuation is generally lower compared to other polarization effects in turbid media and bulk tissues [139].

In many cases, the Mueller matrix of a depolarizer remains diagonal rather than symmetric as in the above two decomposition method. Symmetric decomposition addresses this issue by employing a five factor product decomposition, [117]

$$M = M_{D2} M_{R2} M_{\Delta(diag)} M_{R1} M_{D1} \tag{24}$$

This method may have advantages when investigating depolarizing media with tilted input and output interfaces in which case interface refraction induced diattenuation and retardance match with the equivalent cascade of five elements [29]. It is noted that the symmetric decomposition cannot be applied for a special class of Mueller matrices known as non-Stokes diagonalizable Mueller matrices [117, 140, 141].

5.2 Differential decomposition and root decomposition

Another important recent development was the extension of the differential decomposition method into turbid media polarimetry, which is becoming a complementary alternative to the product decomposition method discussed above. Differential decomposition has been validated in simulations as well as phantom and tissue experiments and has demonstrated advantages for quantifying fundamental polarization properties of many homogeneous samples [118, 121-123, 142].

For a light beam propagating along the z axis, the Mueller matrix $M(z+dz)$ can be written in the form of an iterated differential function as [118]

$$M(z+dz)=U(dz)M(z)=I+mdz \tag{25}$$

where $U(dz)$ is the differential propagation matrix, I denotes an identity matrix as the initial value condition $M(z=0)=I$, and m is the differential matrix with information about the fundamental polarization properties of interest. The equation can also be written as [118],

$$dM / dz=mM \tag{26}$$

If the medium can be assumed to be continuous and has a uniform depolarization distribution over a distance of b along z axis, m is then z independent and can be solved. The solution can be then given by[118]

$$M = \exp(bm)$$
$$m \propto L=\ln(M) \tag{27}$$

b can be regarded as a scalar parameter that does not interfere with the interpretation of m in terms of depolarization, retardance and diattenuation. m can be derived from the matrix logarithm of the Mueller matrix L. The fundamental polarization properties can be determined by constructing the Lorentz anti-symmetric and symmetric components L_m and L_u,[118, 119, 122]

$$L_m = \frac{L - GL^T G}{2}, L_u = \frac{L + GL^T G}{2} \tag{28}$$

G is diag(1,-1,-1,-1) known as the Minkowski metric tensor. For a medium with depolarization, the polarization parameters can be then determined from L_m and L_u, summarised in [119, 143]

Magnitude of diattenuation:

$$D = \tanh[\sqrt{L_m(1,2)^2 + L_m(1,3)^2 + L_m(1,4)^2}]$$

Polarization maintaining power:

$$\Delta = \frac{|a_1| + |a_2| + |a_3|}{3}$$

$$a = L_u(1,1),$$

$$a_1 = L_u(2,2) - a, a_2 = L_u(3,3) - a, a_3 = L_u(4,4) - a$$

Linear retardance:

$$\delta_L = \sqrt{L_m(2,4)^2 + L_m(3,4)^2}$$

Circular retardance:

$$\delta_C = \frac{L_m(2,3)}{2}$$

Magnitude of total retardance:

$$R = \sqrt{\delta_L^2 + 4\delta_C^2}$$

A key physical model that differential decomposition relies on is that the polarization properties of the analysed medium have a uniform distribution along the optical path. It is noted that the root decomposition method [37, 124], which can be regarded as an extended product decomposition method, employs exactly the same model. Hence, the root decomposition and differential decomposition are completely equivalent [120]. The root decomposition can be expressed in the form of a limit as

$$V = \lim_{n \to \infty} n\left(\sqrt[n]{M} - I\right) \tag{29}$$

This limit can be solved analytically,

$$M = \lim_{n \to \infty} \left(I + \frac{1}{n}V\right)^n = \exp(V) \tag{30}$$

$$\Rightarrow V = \ln(M) \equiv L$$

Therefore, V generated from root decomposition is equal to L generated from differential decomposition. The fundamental properties can be interpreted from V in the same way as from L.

The accuracy of the decomposition results depends on how well the medium matches the decomposition method assumptions [120]. When the medium properties are closer to a model that is a cascade of three or five polarizing elements, the factor product based method may be more appropriate. For media with uniformly distributed polarization properties, differential decomposition and root decomposition may demonstrate advantages [123, 143]. Hence, in practice, the selection of decomposition method should be made on a case-by-case basis, especially for biological tissues with complex structures.

5.3 Azimuthal angle insensitive interpretation method

The measured Mueller matrix is dependent upon the azimuthal orientation between the invisible anisotropic axis of tissue and the defined "horizontal" axis of a Mueller matrix, which may lead to variation during inter- and intra-sample measurements. Besides the decomposition methods reviewed in the previous sections,

Mueller matrix transformation techniques have also been introduced recently to address this issue and have been validated and used in a number of biological tissue studies [125-131]. The following rotation-independent parameters were proposed based on experimental data and simulation result analysis

$$A = \frac{2bt}{b^2 + t^2}$$

$$b = \frac{m_{22} + m_{33}}{2} \tag{31}$$

$$t = \frac{\sqrt{(m_{22} - m_{33})^2 + (m_{23} + m_{32})^2}}{2}$$

The parameters A and b are strongly correlated with tissue anisotropy and depolarization respectively [127, 129, 144]. Since only linear polarization is dependent upon the spatial azimuthal angles, these rotation independent parameters were obtained from the top-left 3×3 elements in a Mueller matrix which correspond to linear depolarization transformations. This computationally-light interpretation method would be promising in high resolution real time polarimetric image analysis as well as partial Mueller polarimetry like 3 × 3 Mueller polarimetry.

6. The biomedical applications of Mueller polarimetric imaging

Interpretation of Mueller matrices can improve the understanding of how the fundamental polarization properties of tissue correlate with pathological features in a consistent and reproducible manner, and form a bridge between polarimetric data and clinically meaningful information. Therefore, a number of image contrast mechanisms besides traditional unpolarized radiation intensity have been obtained from Mueller polarimetric imaging, and have a broad range of applications.

It was demonstrated that early stage cancerous human colon is less depolarizing than healthy colon through *ex vivo* measurements with a multispectral Mueller polarimetric imaging system [14]. Using the same system, it was also shown that tissue depolarization could provide useful image contrast to quickly identify the stage of colon cancer development [16], and the relevant histopathological reasons were discussed in terms of tissue layers [17] and tissue absorption and scattering [15]. The system was also found to be a promising tool to evaluate colon cancer progression and residual cancerous tissue after radio-chemical therapy [20]. As displayed in Figure 1(a) which is an illustrative example to exhibit the advantages of polarimetric imaging over polarization insensitive imaging, significant differences in tissue linear retardance and depolarization in healthy and precancerous regions of human cervix were observed [12] and it was noted that cervical tissue depolarization is capable of

revealing morphological changes in the epithelium, with the retardance sensitive to the morphological changes in the stroma [19]. 62% sensitivity and 64% specificity were achieved by optimizing a simple tissue retardance threshold [18]. Another application demonstrated the ability of polarimetry to characterize the micro-organizational state of the myocardium and to monitor regenerative treatments of myocardial infarction [145]. Additionally, by measuring regional birefringence of bladders, organizational anisotropy as a function of distension pressure could be revealed [106, 137], as well as local structural disorders of the bladder wall caused by partial bladder outlet obstruction, as exhibited in Figure 2(d). The retardance contrast between healthy and obstructed regions of the bladder would be potentially useful to guide augmentation surgeries and monitoring the tissue functionality following tissue engineering therapies [21]. Mueller polarimetry or polarimetric imaging has furthermore been used to investigate muscles [146], normal and precancerous human cervix [147], oral [13] and lung tissues [148], radiofrequency ablated porcine myocardial tissue [149], skeletal muscle [150], growth of bacteria colonies [151], skin [152-155] including melanoma [156], animal tissues [144], bladders [137], the orientation of collagen fibres in 3-D space [23], red blood cell suspensions [157], etc.

The majority of the studies mentioned in the preceding paragraph were conducted on bulk tissue in reflection mode, which has significance for *in vivo* tissue diagnosis. A number of applications of Mueller polarimetric imaging are instead based on detecting unstained thin tissue cuts [22, 131, 144, 158-162] in a transmission geometry. Since Haematoxylin and Eosin (H&E) staining and other staining techniques require time and elaborate sample preparation by a well-trained and experienced pathologist for diagnosis, unstained Mueller microscopy may be used for rapid and low cost pathological inspection [159, 160] and instant tissue characterization [136, 163]. As shown in Figure 2(b), polarimetric imaging has been utilized to guide scanning mass spectroscopic analysis of a pathological slide of breast cancer tissue to detect suspicious cancerous regions. Mass spectrometry is able to give quantitative pathological classification but suffers from long acquisition time if used to generate an image. Polarimetric imaging, especially depolarization imaging was demonstrated to be helpful to improve scanning efficiency and significantly shorten the diagnostic time [22]. In Figure 2(c), a pathological slide of a liver sample with fibrosis was imaged by polarimetric microscopy. Compared with the polarization insensitive image on the left, the image on the right was reconstructed based on the retardance and fast axis orientation information of the sample, and is able to significantly enhance the birefringent fibrous structures arising from liver fibrosis [164]. Mueller polarimetry has also been used to study autofluorescence of tissue to differentiate histological biopsy sections of benign (dysplasia) and malignant (adenocarcinoma) uterine cervical tumours [165] and rectal walls [162].

Mueller polarimetric spectroscopy - as an extension to polarized light scattering spectroscopy - can not only provide depolarization spectra that are independent of azimuthal angle, but can also probe additional information about tissue diattenuation and retardance for tissue diagnosis [166]. Mueller matrix descriptions have been extended towards tissue autofluorescence spectroscopy and initially explored for cervical cancerous tissue diagnosis, as shown in Figure 2(e). The additional linear and circular diattenuation spectra possess potential advantages over elastic scattering based approaches. Contrast can be observed between normal and precancerous groups attributed to the loss of anisotropic organization of collagen, which suggests that fluorescence diattenuation and polarizance originating from anisotropic organization of collagen in the connective tissue may serve as potentially useful diagnostic metrics [167].
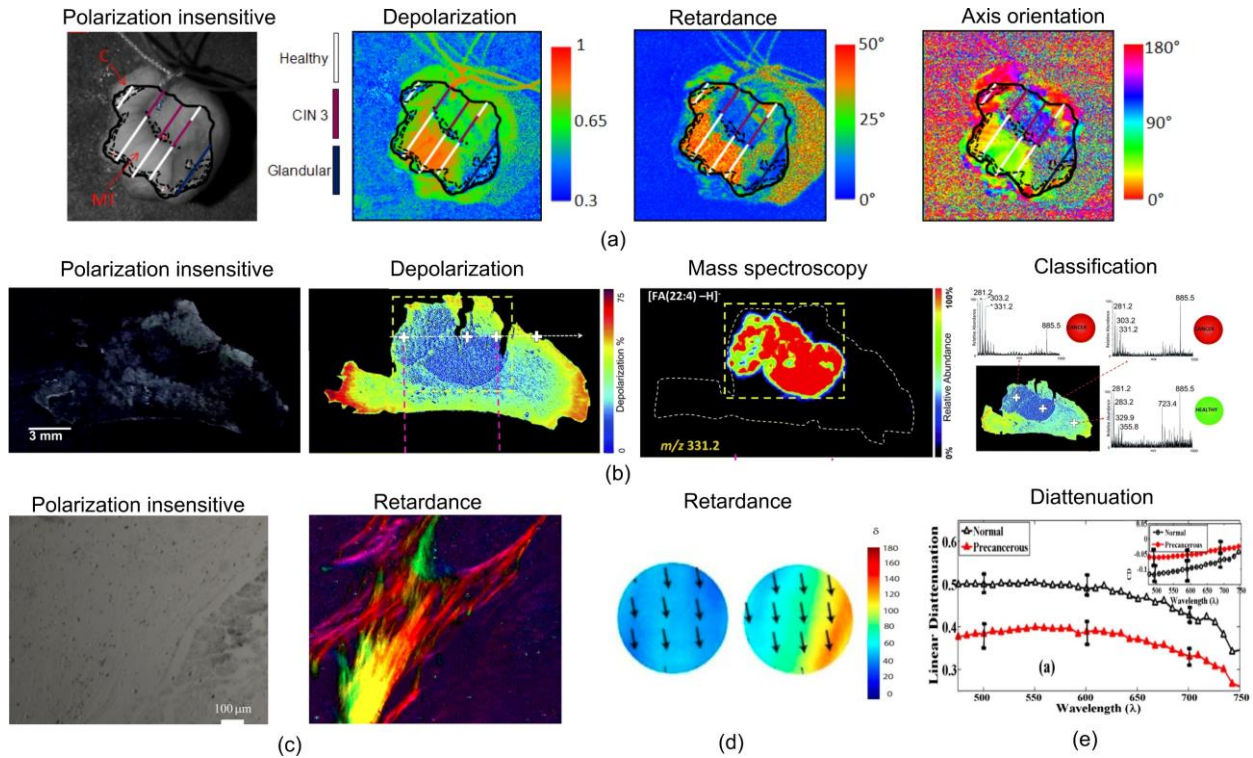
Figure 2 Application of Mueller polarimetry for tissue diagnosis. (a) Human cervical tissue with precancer (CIN3). From left to right are polarization insensitive image, depolarization image, retardance image and fast axis orientation image. The region with CIN3 demonstrated a considerably lower magnitude of retardance than healthy regions. The contrast cannot be observed in the corresponding polarization insensitive image (b) Polarimetry guided mass spectroscopic analysis of a pathological slide of breast cancer. From left to right are polarization insensitive image, depolarization image obtained from complete Mueller polarimetric imaging, scanning mass spectrometry, a demonstration of classification of healthy and cancerous sites. The observed depolarization contrast is likely also influenced by anisotropy (alignment) of the muscle background related to pathological changes of breast cancer. (c) Pathological slide of a liver sample with fibrosis. The left image is polarization insensitive. The right image is reconstructed based on the retardance and fast axis orientation information which significantly enhances the birefringent fibrous structures arising from liver fibrosis. The colorimetric representation strategy is the hue-saturation-intensity visualization scheme (hue=fast axis orientation, saturation=100%, intensity=retardance value). (d) Retardance image of rat bladders. The left image was obtained from a healthy bladder. The right one was from a rat suffering from bladder obstruction. The obstructed bladder demonstrated a high retardance value, which would be useful to guide surgeries and monitor tissue function following tissue engineering therapies. (e) Linear diattenuation spectra of autofluorescence from human cervical tissues. The mean spectra from 15 precancerous [CIN I (four), CIN II (six), and CIN III (five)] and five normal tissue sections are plotted and the error bar is the standard deviation. The inset figure top right shows circular diattenuation spectra. Contrast can be observed between normal and precancerous groups attributed to the loss of anisotropic organization of collagen. The figures were reproduced from [12, 21, 22, 164, 167].

be analysed individually to construct at least 16 linear equations of Mueller matrix elements, denoted by

$$M_{sample}[S_{in1}, S_{in2}, S_{in3}, S_{in4}] = [S_{out1}, S_{out2}, S_{out3}, S_{out4}] \quad (32)$$

7. Design of a Mueller polarimetric imaging system

7.1 Measurement of Mueller matrices

In order to obtain all the elements in a 4×4 Mueller matrix of a sample, at least four linearly independent input Stokes vectors are required and their output Stokes vectors should

As demonstrated in Figure 3, a polarimetric imaging system therefore consists of a light source, a polarization state generator (PSG) to generate required input Stokes vectors S_{in}, a polarization state analyser (PSA, normally called Stokes polarimeter if used alone) to determine the output Stokes vectors S_{out}, and a light detector or image sensor to record all the required states.
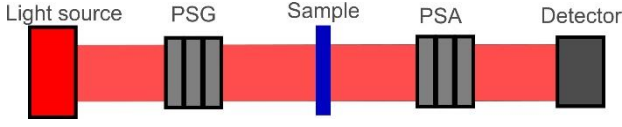
Figure 3 A general configuration of a Mueller polarimeter. A polarimetric imaging system consists of a light source, a polarization state generator (PSG), a polarization state analyzer (PSA), and a light detector or image sensor.

The required input Stokes vectors constitute a matrix represented by M_{PSG}. Equation (32) can be rewritten as

$$M_{sample}M_{PSG} = [S_{out1}, S_{out2}, S_{out3}, S_{out4}] \quad (33)$$

Each output Stokes vector $S_{out\ i\ (i=1,2,3,4)}$ in the right hand part of Equation (33) are obtained from polarization insensitive radiometric intensity measurements $P_{i\ (i=1,2,3,4)}$ by the light detectors or image sensors, via a data reduction matrix M_{PSA}. The process can be described by

$$M_{PSA}[S_{out1}, S_{out2}, S_{out3}, S_{out4}] = [P_1, P_2, P_3, P_4] = P \quad (34)$$

Using Equation (33), Equation (34) can then be expressed by the following linear equation that characterizes the entire process of measurement,

$$M_{PSA}M_{sample}M_{PSG} = P \quad (35)$$

Note that M_{PSG} and M_{PSA} are named the instrumental matrices of the PSG and the PSA respectively in Mueller polarimetry. Thus, the Mueller matrix of the sample is determined by solving Equation (35),

$$M_{sample} = M_{PSA}^{-1}PM_{PSG}^{-1}, \quad (36)$$

Both M_{PSG} and M_{PSA} entail at least four linear independent state vectors such that neither of the ranks of M_{PSG} and M_{PSA} are less than four to ensure this linear equation has a unique solution; that is, P should contain at least 16 the radiometric measurements to solve Equation (35). When M_{PSA} and M_{PSG} satisfy the minimal requirement for the matrices' ranks, but are not square matrices (i.e. P contains more than 16 radiometric measurements), this implies oversampling of the polarimetric system and their inverses should be replaced by Moore–Penrose pseudoinverse matrices M_{PSA} and M_{PSG} defined by

$$A_P^{-1} = (A^T A)^{-1} A^T \quad (37)$$

where A can be replaced by either M_{PSA} or M_{PSG}. The Moore-Penrose pseudoinverse can be considered as computing the least squares solution of Equation (35). An oversampling system may contribute to a reduction of system noise (uncorrelated noise).

7.2 Typical configurations: principles and devices

As pivotal parts of a Mueller polarimeter, the PSG and the PSA are constructed to generate the required input SOPs and analyse the output SOPs so as to solve Equation (35) and obtain the Mueller matrix of the sample. The design of many passive polarization measurement devices like ellipsometers or Stokes vector polarimeters can be directly duplicated for the PSA and PSG. Here we introduce a number of typical architectures for Mueller polarimeters with different PSA and PSG designs.

7.2.1 Fourier modulation techniques

A classical technique of Mueller polarimetry is based on dual mechanically rotated retarders, which may incorporate Fourier analysis as first described by Azzam in 1978 [168], as shown in Figure 4(a). The PSA and the PSG for this kind of configuration is mirror-symmetric but both comprise a fixed linear polarizer and a rotating linear retarder. The two linear polarizers are kept parallel or perpendicular while the two retarders rotate at two different angular rates, for instance one of the optimal ratios for the increments is five to one [168]. Other optimal ratios can be found by condition number based polarimetric system optimization which will be discussed in the next section. The intensity is sequentially sampled during the rotation of the retarders, resulting in a modulated signal, which can be Fourier analysed (Fourier series or Fourier transform), and all the Mueller matrix elements can be derived from the Fourier coefficients. Fourier analysis here serves as an alternative method to the general method based on matrix inverse or pseudoinverse in Equation (36) and (37) to solve Equation (35).

The primary advantages of this dual-rotated-retarder configuration are fewer moving parts, reduced instrumentation cost, and that the calibration can be done without the need for reference samples the following assumptions: 1) both the linear retarders used in the PSG and PSA exhibit no diattenuation and depolarization; 2) the increment of rotation of both the linear retarders is highly reproducible [169, 170]. The disadvantages are the long image acquisition time resulting from the mechanical components and that the signal is usually oversampled. Typical acquisition time for a single one million-pixel radiometric image by a normal image sensor is tens of milliseconds. Time sequential acquisition of the tens or hundreds of images required by this technique can take additional seconds or even minutes. Therefore, although oversampling may reduce uncorrelated system noise, it is generally not an efficient solution for real time polarimetric imaging of moving targets. However, it may suit single-point detection better since single-point detectors like photodiodes and photomultiplier tubes have response time typical in several nanoseconds.

An important extension of Fourier modulation Mueller polarimetry in the past decade is the spectrally encoded snapshot Mueller polarimeter [171, 172] developed based on the channelled spectro-polarimetry technique [171,

173]. In this case, modulation is achieved by non-rotated variable retarders for which the phase retardance is modulated.

Spectrally encoded snapshot Mueller polarimeters take advantage of the wavelength dependant phase retardance of linear retarders (especially in a multiple order linear retarder), and the phase retardance of each retarder in the PSG and PSA is passively modulated in the wavelength domain. A typical snapshot Mueller polarimeter consists of: 1) a 0° linear polariser together with a 45° and 0° linear retarder for the PSG; 2) a 0° and 45° linear retarder together with a 90° linear polariser for the PSA; 3) a spectrometer, as displayed in Figure 4(b). The spectral signal carrying the information about a Mueller matrix is modulated by the thicknesses of the four retarders. With the proper determination of the thicknesses of the four retarders, the various matrix elements are separated into independent channels in the Fourier domain. In detail, the Fourier transform of the spectra creates real and imaginary peaks whose magnitudes are expressed as a linear combination of Mueller matrix elements. One of the optimal choices of retarder thickness is 1-2-5-10. Another choice 1:1:5:5 may also be employed (by using a first order approximation of phase retardance expansion in terms of wavelength).

A crucial assumption of spectrally encoded snapshot Mueller polarimetry is that the sample is achromatic within the working wavelength band in terms of its polarization properties. It is also assumed that all the linear retarders used in the polarimeter exhibit no diattenuation and depolarization. The validity of the former assumption relies on the spectral polarimetric properties of the sample, the spectral bandwidth of light sources employed as well as the spectral resolution of the spectrometer, and it is thus recommended to do spectral analysis before implementing the method. The spectra convey all the polarimetric information for one point on the sample and its Mueller matrix can be recovered via Fourier analysis. It is noticed that even with simultaneous acquisition of 16 Mueller matrix elements, polarimetric imaging may still entail raster-scanning devices or hyperspectral imaging devices, which still fails to avoid time sequential acquisition.
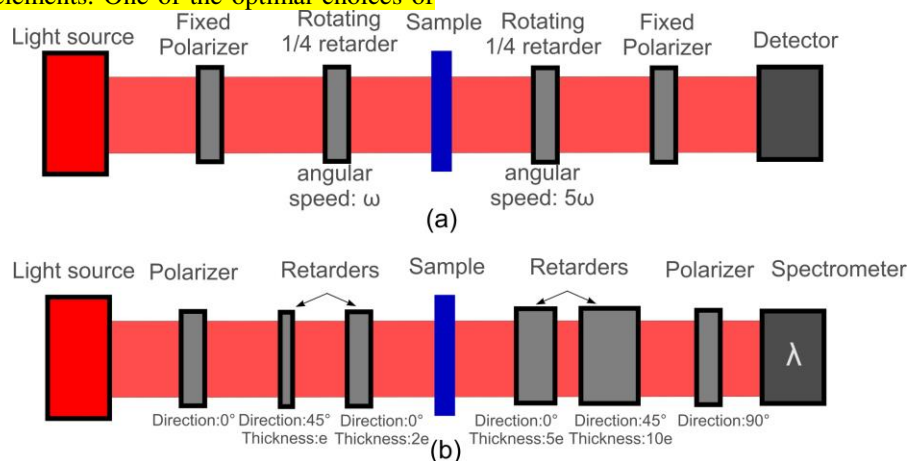

Figure 4. (a) a typical Mueller polarimeter based on dual mechanically rotated retarders. (b) a typical spectrally encoded snapshot Mueller polarimeter.

7.2.2 Non-modulation techniques and variable retarders

Many Mueller polarimeters are not based on modulation techniques and Fourier analysis, but the universal method based on matrix inverse or pseudoinverse in Equation (36) and (37). A typical configuration consists of a PSG and a PSA that have a smaller number of (normally four) states respectively so that only a limited number of (normally 16) measurements are sufficient to solve Equation (35) and obtain the Mueller matrix.

A classic non Fourier modulation based configuration uses a combination of a rotatable or removable quarter waveplate and rotatable linear polarizer to generate or analyse all the elements defining the Stokes vector one by one, namely, "horizontal", "vertical", +45°, -45° linear and left, right circular polarizations. This configuration requires mechanical rotation of both the waveplate and the linear polarizer, or rotation of the linear polarizer and removal of the waveplate [30].

Many non-modulation configurations are based on the application of electronically-controlled variable retarders without any moving parts. A suitable combination of variable retarders and linear polarizers possesses the ability to generate or analyse any polarization state. Typically, two variable retarders and a fixed linear polarizer can be used for a single PSA or PSG, and as a result a Mueller polarimeter needs four variable retarders. There are various types of retarders available with different operating mechanisms. Photo-elastic modulators (PEM) are based on the photo-elastic effect (linear retardance can be controlled by stress) of transparent

materials, induced using a high frequency quartz piezoelectric transducer attached to the end of the material. PEMs have a very high modulation frequency determined by the piezoelectric material in the transducer. They can be applied to Mueller polarimetric imaging, but normally require a high speed camera and small exposure time in scale of microsecond or less, in addition to careful gating and synchronisation [174, 175], which makes it difficult to use sometimes for small numerical aperture systems under relatively weak lighting conditions like endoscopy.

Pockell's cells use the electro-optical effect (linear retardance can be controlled by an external electric voltage in some crystals), but have the disadvantage of a small acceptance angle which limits their wide utilization in imaging applications. Liquid crystal variable retarders modulate the birefringence, although for nematic liquid crystals the response time is sensitive to the thickness with a typical range down to several to tens of milliseconds, much slower than PEMs and Pockell's cells. For ferroelectric liquid crystals which modulate the orientation of the fast axis, the response times are on the scale of tens of nanoseconds with fixed retardance. Liquid crystal retarders are sensitive to temperature and require temperature control units for high precision measurements to prevent interference from room temperature variation, which increases the cost. Most of the commercialised temperature controlled liquid crystal variable retarders also have a limited aperture size. However, these variable-retarder-based configurations have conspicuous advantages over mechanically-moving systems in terms of the response time, accuracy and reproducibility.

7.2.3 Snapshot PSAs

It is noted that the vast of majority of PSGs requires time sequential generation of required SOPs (known as a "division of time" architecture), with the exception of snapshot spectrally encoded Mueller polarimeters mentioned in Section 7.2.1. Nevertheless, a number of schemes for PSAs allow analysis of the emergent four Stokes parameters in a snapshot rather than a series of time sequential measurements, including: 1) employing mutliple beam splitters and four image sensors each of which has distinct polarization analysers, known as a "division of amplitude" architecture e.g. the setup in [176]; 2) employing diffractive optical elements or lens arrays to focus separate parts of the aperture onto separate image sensors or different areas of one image sensor e.g. the setup in [177], known as a "division of aperture" architecture; 3) making pixelated micro-polarizers or micro-retarder arrays directly on the image sensor pixels [178-180] known as a "division of focal plane" architecture. A good summary of these PSA architechtures including their advantages and disadvantages can be found in [181].

7.3 Optimisation

Besides the minimum requirement concerning the rank, how to optimise M_{PSA} and M_{PSG} to minimise the error propagating from the measured radiometric matrix P to the resultant Mueller matrix of the sample M_{sample} during two matrix inversions is another important issue. Normally, it is reasonable to consider M_{PSA} and M_{PSG} separately rather than simultaneously during optimization [182] so that the optimization is simplified to a classical problem about the backward stability of a linear equation. Considering a general linear equation with noise $\Delta \boldsymbol{b}$ added to the known vector $\boldsymbol{b}$,

$$\boldsymbol{x} + \Delta \boldsymbol{x} = A^{-1}(\boldsymbol{b} + \Delta \boldsymbol{b}) \tag{38}$$

How the absolute error $\Delta \boldsymbol{x}$ in the result $\boldsymbol{x}$ is sensitive to $\Delta \boldsymbol{b}$ is determined by the backward stability of the coefficient matrix A. The backward stability of A is dependent upon its orthogonality, indicated by its determinant; a matrix will become more orthogonal as its absolute value of determinant increases, leading to a better backward stability. In polarimetry, the matrix A can be replaced by the PSA and PSG instrumental matrices M_{PSA} and M_{PSG} determined by the state vectors selected. The determinant was first introduced as the parameter to assess the backward stability for polarimetry in [170]. The absolute value of the determinant corresponds to the volume enclosed by the end points of the PSA or PSG state vectors in the Poincare sphere. However, the determinant lacks a quantitative indication of the error and the backward stability of the matrix A is quantitatively assessed by its condition number defined by,

$$cond(A) = \left\| A^{-1} \right\| \left\| A \right\| \tag{39}$$

where $\| \|$ denotes the matrix norm. It is noted that the matrix norm employed to characterize the backward stability and serve as the figure of merit to optimise the M_{PSG} and M_{PSA} in Eq. (10) could be the 1-norm, the 2-norm (Euclidean norm) or the ∞-norm (sup-norm) [170, 183]. Nevertheless, the 2-norm is more frequently used since it is simply the square root of the largest eigenvalue of MM^*, where $*$ stands for the conjugate matrix. The relationship between the relative error and the condition number is given by the inequality [184],

$$\frac{\left\| \Delta \boldsymbol{x} \right\|}{\left\| \boldsymbol{x} \right\|} \le cond(A) \frac{\left\| \Delta \boldsymbol{b} \right\|}{\left\| \boldsymbol{b} \right\|} \tag{40}$$

The random error from radiometric measurement is statistically stable, and the maximum noise level is constrained mainly by the condition number. Thus the system signal-to-noise ratio can be assessed. The Frobenius norm has also been reported to assess the error propagation with the assumption that the noise in the measurement is uncorrelated, resulting in an equal variance [185].

7.4 Calibration

Another essential consideration is calibration of polarimetric systems, a procedure to determine the real M_{PSG} and M_{PSA} which normally deviate from their nominal expectations and may lead to systemic error. There have been several calibration methods developed with various drawbacks such as assumptions or requirement for prior knowledge. For example, Fourier modulation based methods assume that the angular increment of rotating elements is perfect, or that the linear retarders used in the PSG and PSA do not have any diattenuation, or that linear polarizers show no retardance [186, 187]. These assumptions can simplify the calibration procedures - e.g. by avoiding the use of calibration samples - but are not always valid in practice and may result in systematic errors in some situations.

Compain *et al.* proposed an eigenvalue calibration method (ECM) [188] that takes advantage of measuring a set of calibration reference samples so as to obtain a proper set of system responses to construct M_{PSG} and M_{PSA} [182, 188]. A commonly used reference sample set is air (for a null response), a linear polarizer orientated at 0° (defined) and 90° (approximately) for linear diattenuation responses and a quarter waveplate (retardance about 90°) for linear retardance responses with the fast axis orientated at 30° (approximately). The ECM is a popular calibration method in Mueller polarimetry because it requires the fewest assumptions and prior knowledge about the calibration samples, e.g. it is not necessary to precisely know about the retardance and orientation of the calibration waveplate, and the ECM provides the most comprehensive information about the PSG and the PSA in various types of Mueller polarimetric systems [188, 189].

8. Instrumental polarization

It is necessary to take consideration of the polarization properties of optical components and instruments used or altered for Mueller polarimetric imaging, since many of them are not designed for the use of polarization techniques, and the residual instrumental polarization may lead to significant errors if assumed to be highly polarization maintaining by default. Instrumental polarization does not have to be avoided since it can be calibrated in most cases. Nevertheless, depolarization would increase the condition number and reduce the robustness of the polarimetric imaging system and should be minimized. There are a number of factors that can affect the polarization properties of optical components, and are summarized here.

8.1 Materials and strains

Certain common optical materials contain intrinsic birefringence, such as sapphire, ruby, quartz, calcium fluoride and many other crystals. Plastics are widely used optical materials but usually demonstrate strong birefringence arising from the internal strains in the manufacturing process. Similar internal strain is believed to arise during fire-polishing of the surfaces for some uncoated moulded glass lenses with high numerical apertures (NA), e.g. NA=0.5, resulting in radially symmetric, tangentially oriented retardance patterns [190]. This stress birefringence can be relieved by annealing during lens fabrication [190]. External (thermal and mechanical) strains from fastening and mounting are also a potential source of birefringence due to the photo-elastic effect, which cannot be always successfully avoided in a compact optical instrument.

8.2 Refraction and reflection at an interface

Refraction and reflection at interfaces between ambient media and optical surfaces constitute the basis for imaging systems based on geometric optics. In general, this is non depolarizing, but linear diattenuation and sometimes linear retardance are present with values dependent on the incident angle and relative refractive index as derived from Fresnel's equation. With normal incidence, refraction and reflection are completely polarization maintaining for linear and circular polarization. The Mueller matrix of refraction with normal incidence is represented by,

$$M_{refraction} = \begin{bmatrix} 1 & 0 & 0 & 0 \\ 0 & 1 & 0 & 0 \\ 0 & 0 & 1 & 0 \\ 0 & 0 & 0 & 1 \end{bmatrix} \tag{41}$$

When light reflects off a material with higher refractive index than the external medium with normal incidence, by convention, the Mueller matrix of reflection is,

$$M_{reflection} = \begin{bmatrix} 1 & 0 & 0 & 0 \\ 0 & 1 & 0 & 0 \\ 0 & 0 & -1 & 0 \\ 0 & 0 & 0 & -1 \end{bmatrix} \tag{42}$$

The negative signs in m_{33} and m_{44} indicate a "flip" of polarization direction for the incidence 45° (and -45°) linearly polarized light and a "flip" of helicity for circularly polarized light, originating from reflectional symmetric transformation of the coordinate systems during the mirror reflection, as shown in Figure 5. Note that with normal incidence actual polarization direction and helicity do not change during reflection with respect to the world coordinates. The signs can be changed by defining different coordinate positive orientations.
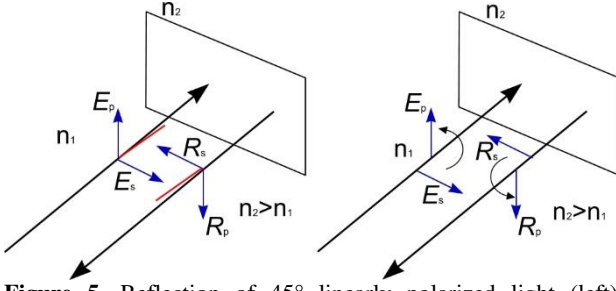
Figure 5. Reflection of 45° linearly polarized light (left) represented by the red line and circular polarized light (right) represented by the curved arrow with normal incidence at an interface with n2>n1. The direction of R_s and R_p are determined according to Fresnel's equation. The actual polarization direction and helicity do not change during reflection with respect to the world coordinates.

As a rule of thumb, many optical systems operating small numerical aperture beams are highly polarization maintaining. With non-normal incidence, the interface always tends to reflect the perpendicular component of electric field to the reflection plane (*s* polarization) more efficiently than the parallel component (*p* polarization), manifesting linear diattenuation, whereas the linear retardance is dependent on the attenuation indices of the materials that are often expressed as the imaginary part of relative refractive index. Low attenuation indices usually correspond to high material transparency, e.g. air, glass, and therefore the attenuation indices of the majority of high transparency optical materials are negligible. Reflection and refraction at the interfaces of materials with negligible attenuation indices are equivalent to linear diattenuators with the diattenuation varying with the incidence angle. The forms of their Mueller matrices are written as,

$$M_{reflect} \propto \begin{bmatrix} a_1^2 + a_2^2 & a_1^2 - a_2^2 & 0 & 0 \\ a_1^2 - a_2^2 & a_1^2 + a_2^2 & 0 & 0 \\ 0 & 0 & -2a_1a_2 & 0 \\ 0 & 0 & 0 & -2a_1a_2 \end{bmatrix}$$

(43)

$$M_{refract} \propto \begin{bmatrix} a_1^2 + 1 & a_1^2 - 1 & 0 & 0 \\ a_1^2 - 1 & a_1^2 + 1 & 0 & 0 \\ 0 & 0 & 2a_1 & 0 \\ 0 & 0 & 0 & 2a_1 \end{bmatrix}$$

$$a_1 = \cos(\theta_i - \theta_r)$$
$$a_2 = \cos(\theta_i + \theta_r)$$

where θ_i and θ_r denote the incidence angle and refraction angle respectively. According to the Mueller matrix of refraction, a single uncoated lens should theoretically demonstrate a small symmetric radial diattenuation increasing with distance from the centre. The diattenuation for lenses with small numerical apertures is normally negligible. For optical systems with high numerical apertures, polarization ray tracing and polarization aberration theory [191-193] are helpful to analyse diattenuation and retardance at the exit pupils. It is noted that high numerical apertures may also result in spatial depolarization.

One special polarization transformation in reflection is total internal reflection which does not reflect *s* and *p* polarizations with unequal efficiency, but merely leads to a phase shift between them. Therefore, total internal reflection is equivalent to a linear retarder in a form of

$$M_{TIR} \propto \begin{bmatrix} 1 & 0 & 0 & 0 \\ 0 & 1 & 0 & 0 \\ 0 & 0 & \cos\delta & -\sin\delta \\ 0 & 0 & \sin\delta & \cos\delta \end{bmatrix}$$

(44)

with the linear retardance δ determined by the incidence angle θ_i and the reflective refractive index n,

$$\delta = 2\arctan\frac{\cos\theta_i\sqrt{n^2\sin^2\theta_i - 1}}{n\sin^2\theta_i}$$

(45)

When the reflective material has non negligible attenuation indices, e.g. metal, reflection leads to linear retardance in addition to linear diattenuation, effectively forming a diattenuated retarder. The linear phase retardance monotonically increases with incidence angle. In Figure 6, the linear retardance and linear diattenuation induced by reflection from an air/aluminium interface and an air/silver interface at 632.8 nm were calculated according to Fresnel's equation. Aluminium and silver are often used in reflecting mirrors including flat and parabolic mirrors. Flat mirrors are normally assumed as an ideal polarization maintaining component to calibrate a polarization system in a reflection mode and it is noted that the assumption is valid at near-normal incidence. The instrumental diattenuation and linear retardance may become an issue when the incidence angle deviates from the normal. An aluminium mirror is also more polarization maintaining at near normal incidence than a silver mirror.
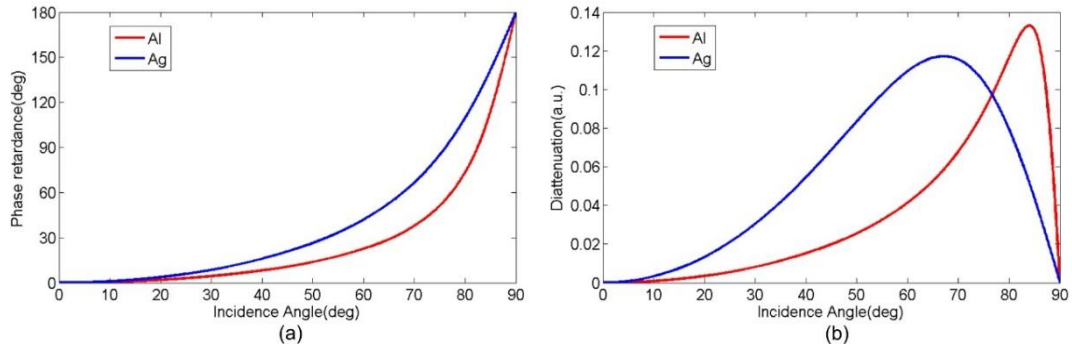
Figure 6 Linear retardance and linear diattenuation induced by reflection from an air/aluminium (Al) interface and an air/silver (Ag) interface at 632.8 nm.

8.3 Thin film coatings

Thin film coatings are widely used to control reflectivity at surfaces of optical elements by utilizing optical interference. The coatings normally cause weak linear diattenuation and weak linear retardance stemming from the coherent superposition of light rays passing through the different layers, in addition to refraction and reflection. The weak linear diattenuation and linear retardance from a single layer antireflection coatings can sometimes be utilised to reduce instrument polarization in optical systems [194]. Residual retardance and diattenuation stemming from thin film coatings cause polarization aberrations [191-193, 195] that are of the fourth and sixth orders with respect to the incidence angle [194].

8.4. Rigid endoscopes

Medical endoscopes are normally long and narrow optical instruments used to observe the interior of a hollow organ or body cavity through small incisions or natural body orifices. They currently play a vital role in screening, diagnosis and surgical treatment of many diseases non-invasively or minimally-invasively. Most modern endoscopes comprise an illumination channel, an imaging channel, and sometimes an irrigation channel and a working channel for the insertion of medical instruments or manipulators. The illumination channel requires high coupling efficiency at the light port and high transmission in the visible range from (the light port at) the proximal end to the distal end of endoscope. The spatial distribution of light radiance illuminating the tissue should also be sufficiently wide and uniform. The most common choice to fulfil these requirements is the incoherent fibre bundle with large individual fibre cores which totally randomise the incident polarization. The Mueller matrix of the illumination channel approximates to an ideal depolarizer in the following form

$$M_{Dep} \propto \begin{bmatrix} 1 & 0 & 0 & 0 \\ 0 & 0 & 0 & 0 \\ 0 & 0 & 0 & 0 \\ 0 & 0 & 0 & 0 \end{bmatrix} \qquad (46)$$

The imaging channel consists of an objective lens with a low numerical aperture, relay optics and an eyepiece. Generally, the objective lens system employs a plane-concave lens to widen the field of view, followed by a positive focusing lens system which is able to make the rays converge, and deliver a demagnified real image to the successive relay optics mounted in a rigid outer tube. The rigid endoscope is preferred for many applications which do not absolutely require bending, e.g. laparoscopic surgery, and has preeminent resolution, wide field of view, wide range of working distances and low chromatic aberrations; properties that are difficult to emulate for flexible endoscopes. Currently the rod lens based rigid endoscope is still the most popular rigid endoscope owing to superior performance, although "chip at tip" devices are increasing in performance and popularity.
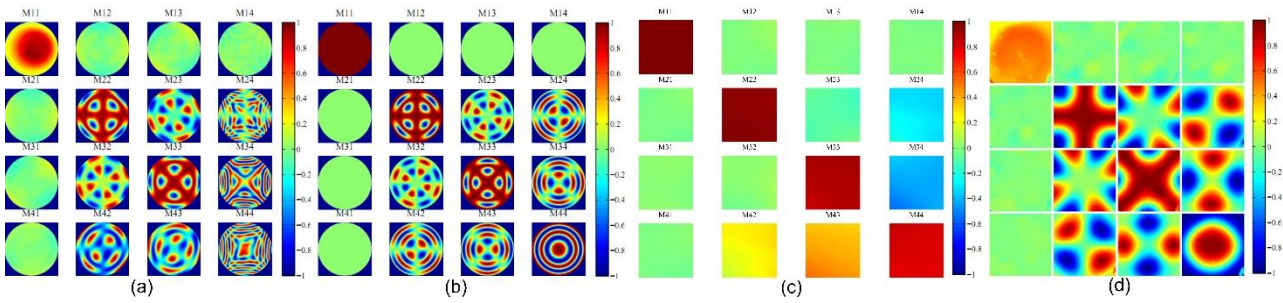
Figure 7 (a) The measured Mueller matrix image of a Karl Storz laparoscope with normal crystal windows [196]. Each elemental image shows one element of the matrix across the whole field of view. The X-shaped artefacts in the in m_{24}, m_{34} and m_{44} are caused by the small acceptance angle of two achromatic quarter waveplates used in the measurement, confirmed by simulation in [196]; (b) the simulated Mueller matrix image of a uniaxial birefringent crystal [196]. The similarity between (a) and (b) indicated that the laparoscope is effectively a uniaxial crystal with the crystal axis parallel to the optical axis of the laparoscope. (c) The measured Mueller matrix image of a Karl Storz laparoscope by replacing the birefringent protective windows with non-birefringent fused silica windows [53, 197]; (d) the measured Mueller matrix image of a GRIN lens [198].

The polarization properties of the imaging channels of rod lens based rigid endoscopes have been investigated experimentally [196]. By measuring the Mueller matrices of laparoscopes from a prominent endoscope manufacturer, Karl Storz GmbH. (Figure 7(a)), it was revealed that a particular laparoscope was effectively a uniaxial crystal with the crystal axis parallel to the optical axis of the laparoscope shown in Figure 7(b), demonstrating spatially varying and symmetric phase retardance, with low diattenuation and depolarization (the X-shaped patterns in m_{24}, m_{34} and m_{44} are ascribed to the small acceptance angle of two achromatic quarter waveplates used in the measurement, confirmed by simulation [196]). The retardance originates from the outer protective windows at both the distal and proximal ends that are made from a birefringent crystal (sapphire). If used in polarimetry, this endoscope would require careful calibration for the highly spatially varying retardance and additional efforts to avoid any small displacement between the endoscope and the image sensor after calibration. The endoscopes with less or no spatially varying retardance are therefore desirable for polarimetric imaging.

A customised laparoscope with the birefringent windows replaced by fused silica was obtained. The Mueller matrices were measured again and displayed in Figure 7(c) [53, 197]. This is equivalent to a linear retarder with low phase retardance (27 degrees). The top left 3×3 sub-matrix essentially demonstrated an identity form, which implies that the polarization properties of the customised laparoscope are not significant and can be called non-polarized or polarization maintaining for linear polarizations. The polarization effects of rigid endoscopes for linearly polarized light can then be removed for linear polarization imaging by simply replacing their crystal windows with non-birefringent material. Such endoscopes would simplify and reduce the requirements for the design of the PSA since the PSA does not have to be miniaturised to match the dimensions of endoscopic tip.

8.5 GRIN lenses

Gradient index (GRIN) lenses can also be used as endoscopic relay lenses, although producing colour images is challenging due to the excessive dispersion of GRIN lenses. However, they offer advantages when working in environments requiring extremely small dimensions, since a GRIN lens can be manufactured down to 0.2 mm in diameter [199]. The Mueller matrix of a GRIN lens was measured in [200] and is reproduced in Fig. 5(d) and is similar to a conventional Karl Storz laparoscope but with fewer orders in the conoscopic interference pattern. Therefore, a GRIN lens is also equivalent to a uniaxial crystal with the crystal axis parallel to the optical axis of the lens, with low diattenuation and depolarization. Such a GRIN lens has been optimised and used as a point detection-based snapshot Stokes polarimeter [200, 201]. It was also altered to become a Stokes polarimetric imaging device with the conoscopic interference pattern removed by a pre-determined matrix division procedure [198].

8.6 Single mode fibres

From the perspective of polarimetry, realistic single mode fibres are strongly birefringent and weakly diattenuating. A circularly symmetric design for single mode fibres would be perfectly polarization maintaining (without any birefringence and diattenuation), and the Mueller matrix would be represented by an identity matrix. However, there exist many random symmetry-breaking imperfections in a fibre including the geometric asymmetry (e.g. slightly elliptical cores) and intrinsic mechanical stress induced by the fibre manufacturing process, as well as extrinsic stresses induced by bending, twisting, squeezing, temperature changes and other effects [202]. These asymmetries cause that two orthogonal polarizations of the fundamental mode (HE11) to

propagate with different velocities, known as polarization mode dispersion (PMD) [203]. In high speed fibre optic communications, PMD causes pulse broadening, leading to an increase in bit-error rate. The effect for polarimetry is that a single mode fibre is birefringent and behaves similarly to a phase retarder. The polarization properties may be controlled by bending, twisting and squeezing the fibre, which is the basis of fibre polarization controllers. Generally, the phase retardance is proportional to the curvature of bending and applied squeezing pressure, and the orientation of effective optic axis is controlled by subtle twist so as to construct an equivalent fibre optic Soleil-Babinet compensator. For a silica fibre bent into a single loop, the phase retardance is specified by,

$$\phi(Radians) = \frac{2\pi^2 a d^2}{\lambda D} \tag{47}$$

where d is the diameter of the fibre, D is the diameter of the loop, λ is the wavelength, and a is a constant (1.33 for silica) introduced by the photoelastic effect.

The asymmetries of fibres also cause the differential absorption of light for the two orthogonal axes, known as the polarization dependant loss (PDL) in fibre optics. PDL exactly corresponds to diattenuation in polarimetry and can be determined directly by Mueller polarimetry. It is worth mentioning that 'polarization maintaining' fibres (PM fibres) are actually not strictly polarization-maintaining. A systematic high birefringence is intentionally introduced in PM fibres so that the birefringence generated by the random asymmetries is almost negligible compared to the systematic birefringence, and the systematic birefringence prohibits coupling between the two orthogonal principle polarization directions. Therefore a PM fibre can only maintain two linear polarization states along the two orthogonal principle polarization directions of the fibre.

9. Mueller polarimetric endoscope and fibre Mueller polarimeter

Mueller polarimetric imaging has enormous potential for tissue sensing and characterization. The technique is strongly desirable for further validation in the form of preclinical trials and clinical pilot studies. However, this technique has not progressed into an *in vivo* stage. A primary obstacle is the lack of a suitable endoscopic system to implement Mueller polarimetric imaging. Such a system would normally require endoscope-compatible designs of the PSG and the PSA, which may be highly complex and expensive. The utilisation of an endoscope with non-polarized imaging channel will be able to simplify the design of the PSA, which will allow the analysis of tissue reflectance SOPs at the proximal end of the scope without complex miniaturization [53, 196]. However, since the illumination channel depolarizes the incident light significantly, one solution would be to only miniaturize the PSG and place it at the distal end.

9.1 3 × 3 Mueller polarimetric endoscope

In one approach developed by the authors [94], 3×3 Mueller polarimetry was used to measure the top left 3×3 sub-matrix of a complete 4×4 Mueller matrix, which is capable of revealing a large proportion of useful polarization information. 3×3 Mueller polarimetry can be implemented involving linear polarization alone and therefore simplifies the system design and the measurement procedures by obviating the need for phase retarders. 3×3 Mueller polarimetry was first adopted for a Mueller polarimetric endoscope to detect tissue linear depolarization and retardance, the most noticeable polarization parameters. A ring shaped linear polarizing film shown in Figure 8 was fixed on the top of the distal end of the illumination channel (double crescent shaped as displayed in Figure 8(a)). The full miniaturization of the PSG was avoided by rotating the endoscope to generate 0°, 45° and 90° linear polarized light. The backscattered light from the tissue was imaged through the nearly polarization maintaining rigid endoscope to the linear PSA at the proximal end. A typical acquisition time of a Mueller polarimetric image using this endoscope is 11.6 s. It is noted that the angle of view, the working distances of this polarimetric endoscope is not affected by the polarimetric devices, but mainly determined by the laparoscope employed. The angle of view of the laparoscope was about 70° and its working distance ranges from 0.5 cm to over 15 cm. The digital resolution of the system is dependent on the CCD camera used.
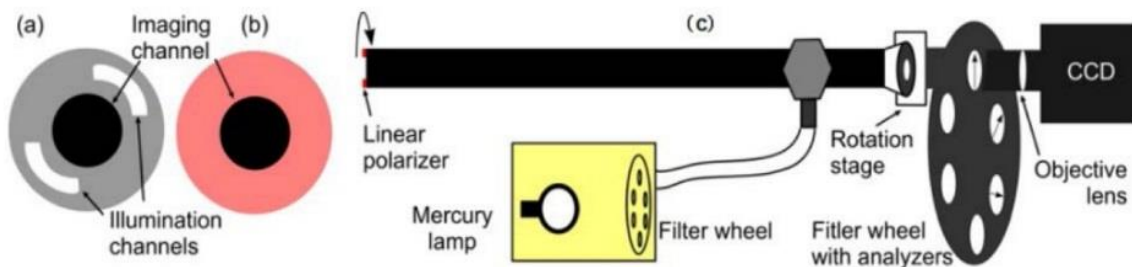
Figure 8. A 3 × 3 Mueller polarimetric endoscope. (a) View of the distal end of endoscope. (b) Ring shaped linear polarizing film covering illumination channel. (c) Side-view of the endoscope. The figure was reproduced from [94].

The acquired 3×3 Mueller polarimetric images were interpreted using a similar method to polar decomposition for a complete Mueller matrix [204]. As a result, linear depolarization, retardance and linear diattenuation can be obtained to reconstruct images. The abdomen of a rat was imaged using this endoscope and one set of results is displayed in Figure 9. The organs can be discriminated based on their different polarization properties, for example, the liver demonstrated a remarkably low depolarization (represented by a high polarization maintaining power in Figure 7 (b)) because the liver contains the most blood of all the imaged organs. The multiply scattered light undergoes strong absorption by haemoglobin at 546 nm. The polarized singly scattered light take up the largest portion of total reflectance and hence the liver presents a highest polarization maintaining power. In contrast, since haemoglobin does not absorb as much at 628 nm as it does at 546 nm, the polarized incidence can be further depolarized and backscattered by deeper tissue resulting in a low polarization maintaining power. The stomach showed different retardance to the other organs at both the wavelengths. The distinguished retardance property of the stomach might be related to the very thick muscular layer in stomach which is birefringent.

It is noted that there are some underlying assumptions that were not fully addressed in the first paper introducing the interpretation method of 3×3 Mueller matrices in [204]. Firstly, the circular diattenuation should be known or otherwise could be assumed to be zero; secondly, the depolarization matrix has to be in a diagonal form; thirdly, the linear depolarization for 0°/90° and -45°/+45° should be identical. The assumptions - especially the latter two - cannot be satisfied in many cases, especially for anisotropic tissues. Based on Monte Carlo simulation and tissue phantom studies, Wang *et al.* assessed the difference between the results obtained from 3×3 Mueller matrix decomposition [204] and 4×4 Mueller polar decomposition [205], and found that the parameters derived from the 3×3 Mueller matrix decomposition are usually not the same as those from the 4×4 Mueller matrix decomposition but demonstrate similar qualitative relations to changes in the microstructure of the sample, such as the density, size, and orientation distributions of the scatterers, and birefringence of the interstitial medium. Another emerging interpretation method named "Mueller matrix transformation method" introduced in Section 5.3 may be more promising to extract the useful linear depolarization and retardance related information of tissue from 3×3 Mueller matrix images.
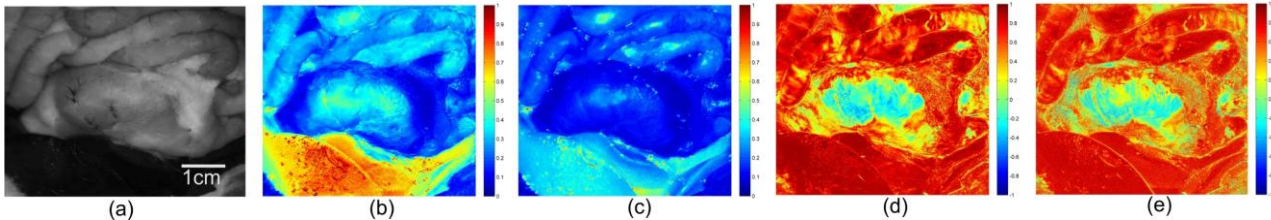

Figure 9. (a) Unpolarized image of a rat abdomen, small bowel (red arrows), stomach (purple arrows), liver (white arrows) and fat (blue arrows). (b) linear polarization maintaining power image at 546 nm (c) linear polarization maintaining power image at 628 nm. Linear retardance at (d) 546 nm and (e) 628 nm (represented by the cosine of linear phase retardance value). The images show a field of 5.5 cm × 5.5 cm with a working distance of 5 cm. The figure was reproduced from [94].

The optimization of the PSG and PSA for 3×3 Mueller polarimetry can be based on maximizing the determinant and minimizing the 2-norm condition number of their instrumental matrices. In our later study [197], we showed that one set of optimal configurations is obtained when the PSG generates 0°, 60° and 120° linearly polarized light with 0°, 60° and 120° linear polarizers as analysers in the PSA.

9.2 Complete Mueller polarimetric endoscope

4×4 Mueller polarimetry was also achieved in our previous work [137, 206] by using a rotating endoscope sheath as shown in Figure 9. A ring shaped horizontally positioned linear polarizing film was attached on the

illumination channel of the stationary laparoscope. At the distal end of the sheath, a ring shaped rotatable quarter retarding film was mounted. The rotation of the sheath was controlled by a motorised rotation stage at the proximal end of the laparoscope. The fast axis of the rotatable retarding film was selected to be -45°, 0°, 30° and 60° in order to generate the optimal polarization states according to the optimisation done for a rotating-retarder Stokes polarimeter in [183]. A free-space PSA was used at the proximal end of the endoscope. The free-space PSA and the endoscope, which was effectively a linear retarder, can be considered as an endoscopic PSA. A typical acquisition time of a Mueller polarimetric image using this endoscope is about 30 seconds due to the slow rotation stage and a slow time sequential PSA. A much faster Mueller polarimetric endoscope system based on a

non-time sequential PSA and a PSG based on a faster motor can potentially work in real time. It is noted that the angle of view, the working distances of this polarimetric endoscope is also mainly determined by the laparoscope employed, and the digital resolution of the system is also dependent on the CCD camera.

This complete Mueller polarimetric endoscope (MPE) has been used to image a porcine bladder tissue in high definition [137]. As shown in Figure 10, the endoscope comprehensively characterized polarization properties of a stretched porcine bladder by measuring Mueller matrices, and thus provided a number of useful image contrast mechanisms besides traditional unpolarized radiation intensity, including linear depolarization, circular depolarization, crossed-polarization, birefringence and the fast axis orientation. Figure 10(h) demonstrates that image contrast was enhanced by the circular depolarization (second column), linear depolarization (third column) and crossed-polarization (fourth column) images compared to the polarization insensitive image (first column) in two representative sub-regions indicated by the squares in Figure 10(d). In the upper sub-region, the fibrous structures could hardly be observed in the polarization insensitive image, but could be easily distinguished in the depolarization and crossed-polarization images due to polarization gating effect introduced earlier. The fibrous structures observed in depolarization were mainly distributed near the tissue surface, and those in the cross polarization image were in deeper tissue. The image contrast was also quantified according to the grey-level co-occurrence matrix method [207] and image gradient assessment over the bladder sample, and a remarkable rise of image contrast by depolarization and crossed-polarization images were further confirmed.

The serosa of the bladder imaged here is known to consist mainly of collagen and elastin fibrils according to second harmonic generation microscopy [21] and electronic microscopy studies [208]. Structures consisting of birefringent collagen and elastin, that cannot be visualized by traditional unpolarized endoscopes, have a critical role in detection of epithelial cancer, obstructive disease of bladders [21], etc. The total phase retardance arising from the bladder serosa was successfully observed and appeared to be spatially varying. A high retardance normally corresponds to well organized (aligned) fibrils. The fast axis orientation image is mainly related to the spatial orientations of fibrils. A continuous rise of retardance and an increasingly uniform distribution of fast axis orientation were also observed when stretching the bladder, because the spatially disordered anisotropic micro-structures of collagen and elastin become better aligned due to the applied one dimensional mechanical force in the stretching process (recorded in a video shown in the original paper). These subtle changes were apparently not detectable by polarization insensitive imaging.
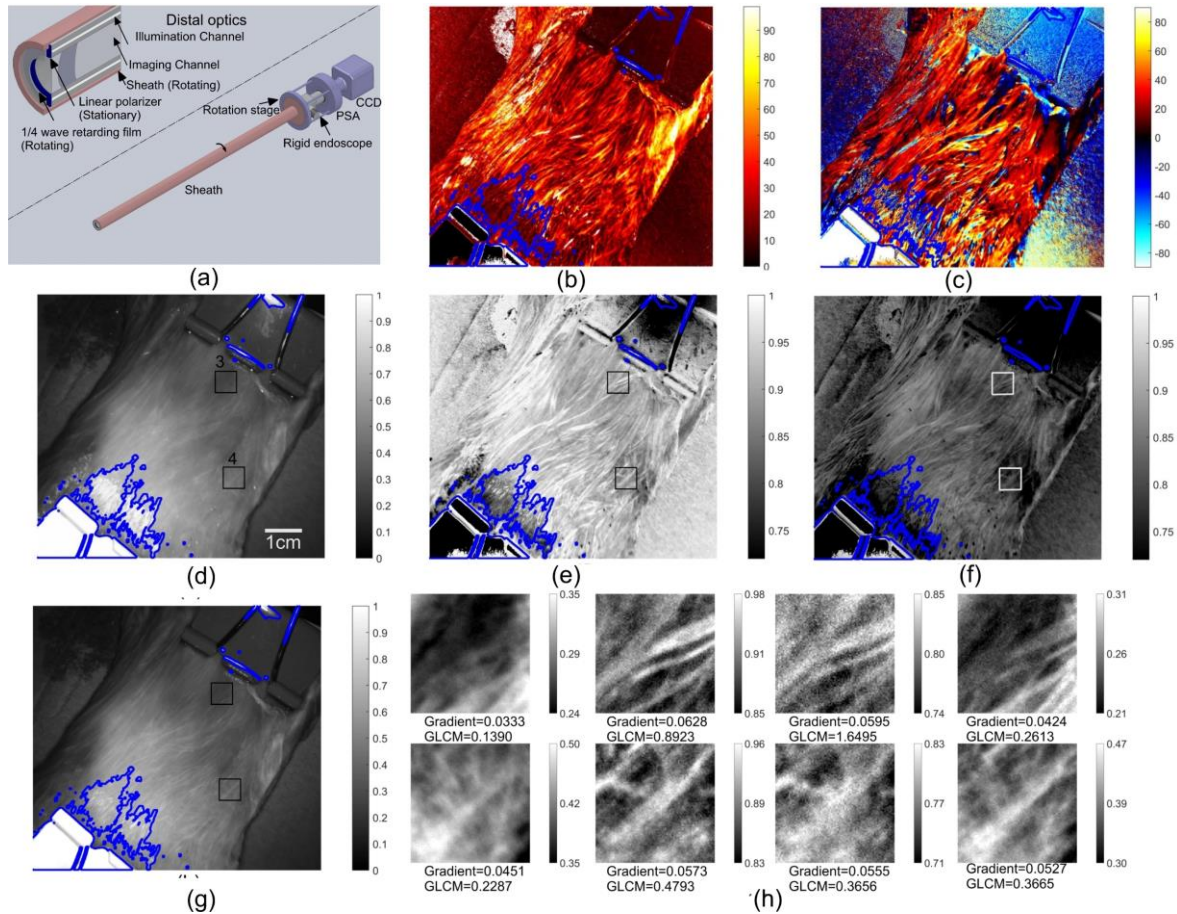
Figure 10. A high definition 4 × 4 Mueller polarimetric endoscope (MPE). (a) The Mueller polarimetric endoscope consists of a stainless steel sheath, a motorised rotation stage, a rigid endoscope, a polarization state analyser (PSA) and a CCD image sensor. The part that rotates during acquisition is represented in red, and the stationary part is in purple. (b) retardance image, (c) the fast axis orientation image, (d) polarization insensitive image for comparison, (e) circular depolarization, (f) linear depolarization images, and (g) crossed-polarization image of the stretched porcine bladder. (h) As an example to illustrate image contrast enhancement, the unpolarized (first column), circular depolarization (second column), linear depolarization (third column) and crossed-polarization (fourth column) images of two representative sub-regions indicated by the squares in (d) were demonstrated. Image contrast was quantitatively assessed by employing two metrics – the grey-level co-occurrence matrix analysis (GLCM) [207] and the mean value of image gradient magnitudes that can be used to denote sharpness of texture in the image. The image contrast values calculated with the two metrics are displayed below each sub-image in (h), and higher values are superior. (b, c, e, f) were obtained by decomposing the Mueller polarimetric images. The areas enclosed by blue lines are affected by pixel saturation and are invalid. (b-g) shows an area about 7.8 cm × 7.8 cm with the working distance 8 cm. The figure was reproduced from [137]

9.3 Polarimetric endoscopes based on stereo-endoscopes

Stereo-endoscopes make use of two separate imaging channels to provide surgeons with stereo vision during minimally invasive surgery. The two imaging channels can be used to acquire images in parallel, e.g. snapshot co-polarized (CO) and cross-polarized (CR) images with respect to illumination polarization, and therefore demonstrate inherent advantages to accelerate acquisition speed for polarimetric imaging. Such an endoscope has been constructed in [51], as shown in Figure 11 (a, b), and

was used to improve the image contrast in narrow band imaging procedures. This polarization endoscope can be used for real time polarization imaging. The *in vivo* results were obtained during a surgical procedure on a porcine subject. The depolarization image was constructed by using the equation (CO-CR)/(CO+CR) convey information about superficial tissue. The CR image conveyed information about deeper tissue. The porcine bladder tissues showed wavelength dependent variations and an increase of superficial blood vessel visibility under polarized detection because the high absorption of haemoglobin in the vessels leads to shorter pathlengths of

backscattered light, resulting in a much lower depolarization, as demonstrated in Figure 11(c). The system was further developed to allow for the detection of the top left 2×2 Mueller matrix elements at video rate [52].
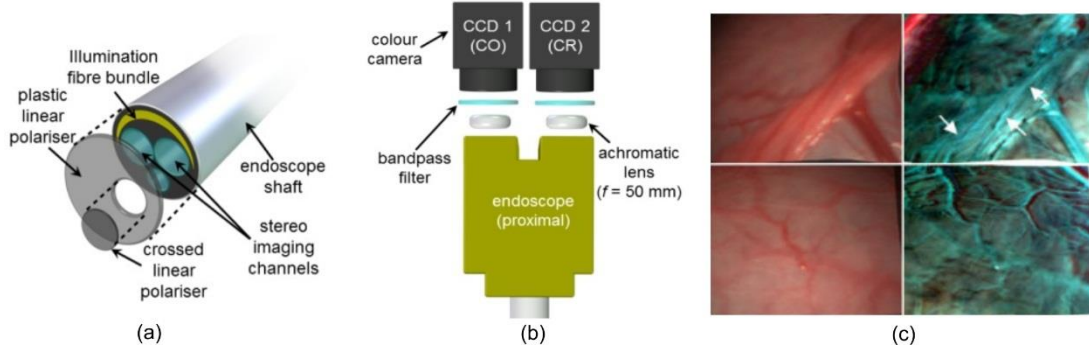

Figure 11 Polarized stereo-endoscope. (a) Tip optics. A linear polarizer placed over the endoscope face generates linear polarized light. The co-polarized (CO) component is detected through the right channel while a separate section with its polarization axis orthogonal collects cross-polarized (CR) light, (b) proximal optics. Bandpass filters and colour cameras were used for *in vivo* narrow band imaging. (c) Standard colour (left column) and pseudo-RGB-colour images reconstructed from tissue polarization information (right column) of porcine bladder. The values assigned in the red channel represent the signal from deep structures conveyed by CR image and those assigned in blue/green channels corresponde to more superficial tissue conveyed in (CO-CR)/(CO+CR) image. White arrows indicate vascular features whose visibility has been enhanced based on a Weber contrast measurement. The figure was reproduced from [51]

9.4 Single mode fibre based laser Mueller polarimeter

A single mode fibre Mueller polarimeter was first demonstrated in [209], by assuming that a single mode fibre is a pure retarder containing constant linear retardance and circular retardance, but no depolarization and diattenuation (no PDL). In our opinion, the assumptions are reasonable if relatively short fibres (e.g tens of centimetres) resulting in negligible PDL and a light source with small bandwidth (e.g. lasers) resulting in minimal spectral depolarization are employed in the system. The technique is based on two subsequent Mueller matrix measurements: a calibration measurement and a sample measurement, and it is also assumed that there is no bending and twisting that may strongly affect the PMD (or retardance property) of the single mode fibre during measurements so that the parameters obtained from the calibration remain the same during the sample measurements.

In the calibration measurement, a fibre double-pass Mueller matrix was recorded by placing a mirror at the distal end of the fibre. The Mueller matrix of the first forward pass through the fibre can be represented by a retardance matrix containing both linear and circular retardance, expressed by

$$M_{SMF\_f} = M_R = \begin{bmatrix} 1 & 0 \\ 0 & m_{R\_f} \end{bmatrix}$$

$$m_{R\_f} = m_{LR}m_{CR}$$

$$= \begin{bmatrix} Rot(-2\varphi) & 0 \\ 0 & 1 \end{bmatrix}\begin{bmatrix} 1 & 0 \\ 0 & Rot(\delta_L) \end{bmatrix}\begin{bmatrix} Rot(2\varphi) & 0 \\ 0 & 1 \end{bmatrix}\begin{bmatrix} Rot(\delta_C) & 0 \\ 0 & 1 \end{bmatrix}$$

$$Rot(x) = \begin{bmatrix} \cos x & \sin x \\ -\sin x & \cos x \end{bmatrix}$$

(48)

The second (backward) pass is then represented by

$$M_{SMF\_b} = \begin{bmatrix} 1 & 0 \\ 0 & m_{R\_b} \end{bmatrix}$$

(49)

$$m_{R\_b} = \begin{bmatrix} Rot(-\delta_C) & 0 \\ 0 & 1 \end{bmatrix}\begin{bmatrix} Rot(-2\varphi) & 0 \\ 0 & 1 \end{bmatrix}\begin{bmatrix} 1 & 0 \\ 0 & Rot(\delta_L) \end{bmatrix}\begin{bmatrix} Rot(2\varphi) & 0 \\ 0 & 1 \end{bmatrix}$$

The double pass Mueller matrix can thus be written as

$$M_{calibration} = M_{SMF\_b}M_{SMF\_f} = \begin{bmatrix} 1 & 0 \\ 0 & m_{R\_b}m_{R\_f} \end{bmatrix}$$

(50)

As a rotation matrix, *Rot(x)* is orthogonal, so the bottom right part of the matrix in Equation (50) becomes

$$m_{R\_b}m_{R\_f} = \begin{bmatrix} Rot(-2\varphi-\delta_C) & 0 \\ 0 & 1 \end{bmatrix}\begin{bmatrix} 1 & 0 \\ 0 & Rot(2\delta_L) \end{bmatrix}\begin{bmatrix} Rot(2\varphi+\delta_C) & 0 \\ 0 & 1 \end{bmatrix}$$

(51)

Therefore, double-passing a single mode fibre is effectively a linear retarder with linear phase retardance δ_L and the fast axis orientation ($2\varphi+\delta_C$). Since a fibre double-passing Mueller matrix has been obtained in this calibration measurement, the linear retardance δ_L and the summation of the fast axis orientation(×2) and circular retardance of the single mode fibre ($2\varphi+\delta_C$) can be

In the sample measurement, the measured Mueller matrix M_m at the proximal end is determined by

$$M_m = M_{SMF\_b}\, M_s\, M_{SMF\_f} \qquad (52)$$

where M_s denote the Mueller matrix of the sample investigated. With Equation (48), (49) and (52), the following equation can be derived,

$$\begin{bmatrix} 1 & 0 & 0 \\ 0 & Rot(2\varphi) & 0 \\ 0 & 0 & 1 \end{bmatrix} M_s \begin{bmatrix} 1 & 0 & 0 \\ 0 & Rot(-2\varphi) & 0 \\ 0 & 0 & 1 \end{bmatrix} = \begin{bmatrix} 1 & 0 & 0 \\ 0 & 1 & 0 \\ 0 & 0 & Rot(-\delta_L) \end{bmatrix} \begin{bmatrix} 1 & 0 & 0 \\ 0 & Rot(2\varphi+\delta_C) & 0 \\ 0 & 0 & 1 \end{bmatrix} M_m \begin{bmatrix} 1 & 0 & 0 \\ 0 & Rot(-2\varphi-\delta_C) & 0 \\ 0 & 0 & 1 \end{bmatrix} \begin{bmatrix} 1 & 0 & 0 \\ 0 & 1 & 0 \\ 0 & 0 & Rot(-\delta_L) \end{bmatrix} \qquad (53)$$

With the δ_L and $(2\varphi+\delta_C)$ obtained in the calibration measurement, the right part of Equation (53) can be calculated. The Mueller matrix of the sample M_s cannot be fully determined due to the unknown fast axis orientation φ of the fibre, but it turned out that the effect of this unknown φ is equivalent to a rotation of the measured sample on the sample plane. Therefore, this does not affect absolute values of polarimetric parameters of the sample, except its absolute orientation axis values. This fibre Mueller polarimeter was validated by sensing a rotating waveplate on the top of a mirror as shown in Figure 12(b).

This technique allowed Mueller polarimetry to be implemented through a flexible optical fibre for the first time and the acquisition of Mueller matrices for non-depolarizing samples was demonstrated. It is a point-detection technique and would need a scanning system to form images. It is also noted that a coherent light source (a laser) was employed in this polarimeter to guarantee the coupling efficiency. Therefore, this fibre polarimeter has to be used carefully due to the presence of speckle. It is known that a single mode fibre has a small core diameter of typically several microns. This diameter could be smaller than a speckle size induced by a laser backscattered from tissue, and as a result, the measured DOP of the emergent light from the tissue might be always close to 1 rather than being sensitive to tissue depolarization properties.
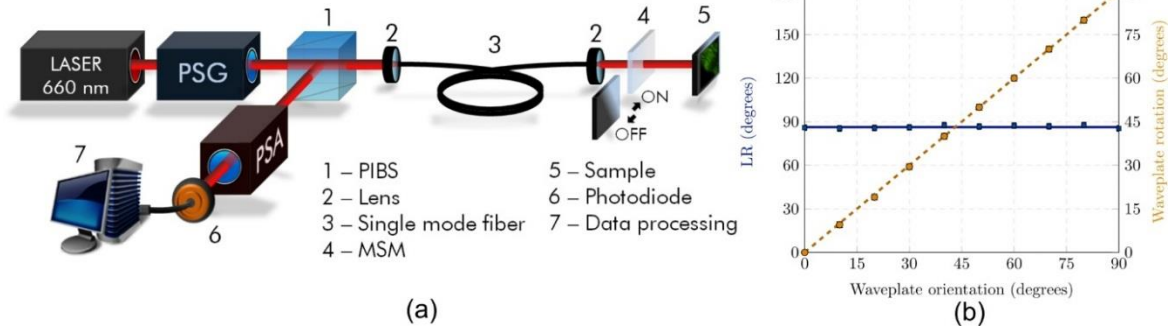

Figure 12. (a) Schematic of the single mode fibre Mueller polarimeter. (PIBS: Polarization Insensitive Beam Splitter; MSM: Micro-Switchable Mirror; PSG: Polarization State Generator; PSA: Polarization State Analyser). (b) The validation results by sensing a rotating waveplate sample on the top of a mirror. The vertical axis denotes linear retardance. The figure was reproduced from [209]

9.5 High speed single mode fibre Mueller polarimeter

The fibre Mueller polarimeter mentioned in Section 9.4 was constructed based on tuneable ferroelectric liquid crystals. It took 70 ms for a single measurement of a Mueller matrix [209], which is not compatible with the demands of modern fast raster scanning systems for imaging [210]. Moreover, bending and twisting of the fibre are essential for endoscopic applications, and as reviewed in the last section, the PMD of a single mode fibre is extremely sensitive to bending and twisting of the fibre which may invalidate the crucial assumption that the linear retardance and circular retardance of the fibre should be unchanged.
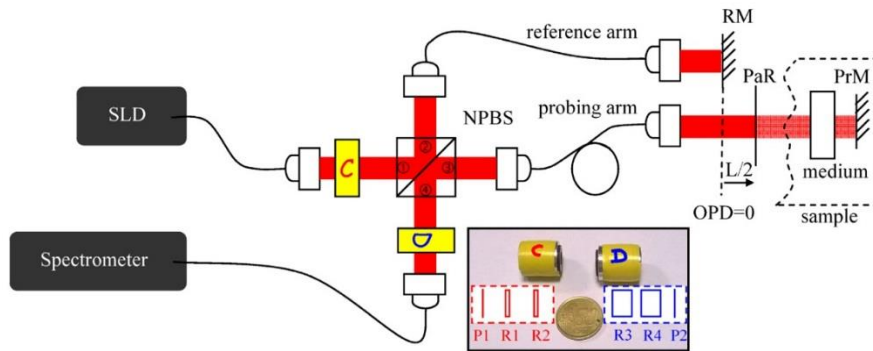
Figure 13. Schematic of the high speed single mode fibre Mueller polarimeter. (SLD: super luminescent diode, C: passive polarization state coding block, D: passive polarization state decoding block, NPBS: non-polarizing beam splitter cube, RM: reference mirror, PaR: 50% partial reflector, PrM: probe mirror. or the Coding and Decoding blocks, P1, P2: linear polarizers are crossed, R1, R2, R3, R4 are retarders oriented respectively at 45°, 0°, 0° and 45° according to the orientation of P1). The figure was reproduced from [210]

The issue was recently addressed by Rivet *et al.* [210]. A spectrally encoded snapshot Mueller polarimeter was converted into a high speed single mode fibre Mueller polarimeter in this work [210]. As discussed in the previous section, for a spectrally encoded snapshot Mueller polarimeter, the phase retardance of each retarder in the PSG and PSA is passively modulated in the wavelength domain, rather than actively modulated by rotation of retarders in the time domain, so the time sequential PSA and PSG in Section 9.4 were replaced by the retarder plates of the coding and decoding blocks as shown in Figure 13.

The technique is the same as Section 9.4, also based on two Mueller matrix measurements: a calibration measurement and a sample measurement procedure. Nevertheless, these two necessary Mueller matrix measurements were conducted simultaneously, and were recorded in one spectrum by the spectrometer. Calibration signals and backscattering signals from the sample were distinguished by making use of the coherence gating technique. A low coherence light source (a super-luminescent diode) was employed in this work for coherence gating.

In detail, there were in total three components to the light signal: 1) the light that passed forwards through the reference arm, was reflected by a mirror ('RM' in Figure 13), then passed back through the reference arm; 2) the light that passed forwards through the probe arm, was reflected by a partial reflector at the distal end of the fibre ('PaR' in Figure 13), then passed back through the probe arm; 3) the light that passed forwards through the probe arm, transmitted through the partial reflector, backscattered from the sample, and passed back through the probe arm. The optical pathlength difference (OPD) between component 1 and component 2 was adjusted to be smaller than the coherence length of the source to create interference, while the OPD between components 1 and 3 was beyond the coherence length. This interference appeared in the high frequency region of the Fourier domain of the spectrum, and conveys information about

the Jones matrices for double-passing the probe and reference arms. It is noted that the Jones matrix for double-passing the reference arm could be predetermined, which allowed the Jones matrix for double-passing the probe arm to be obtained, which corresponds to the calibration measurement in Section 9.4. Therefore, the linear retardance δ_L and the summation of the fast axis orientation (×2) and circular retardance of the single mode fibre $(2\varphi+\delta_C)$ of the probe arm can be calculated. The backscattered signals represented by component 3 corresponded to "the sample measurement" in Section 9.4. This signal did not interfere with components 1 and 2, so it appeared in the low frequency part of the Fourier domain of the spectrum. The Mueller matrix of the sample can thus be determined according to Equation (53). In this way, the two time sequential Mueller matrix measurements (calibration and sample measurements) in Section 9.4 were substituted by a simultaneous measurement of the wavelength spectrum. The Mueller matrix of the sample and the single mode fibre in the probe arm can thus be obtained at the same time (via Fourier analysis of the spectrum specified in spectrally encoded snapshot Mueller polarimetry [171, 172]).

This polarimeter was validated using linear polarizers and waveplates. It is found that the retardance and the diattenuation of the components for validation can be more accurately extracted than depolarization. The technique achieved an acquisition rate as high as 70 kHz and is tolerant to fibre perturbations during acquisition, which is a significant step to develop a raster-scanning probe for Mueller polarimetric imaging. It is still assumed that all the optical elements (except the coding and decoding retarder plates) are achromatic and that the single mode fibre is a retarder without diattenuation and depolarization. The dispersion of the fibre can induce spectral depolarization and may invalidate the assumption that SMF is a pure retarder, leading to depolarization errors [210]. The polarimeter will be tested with scattering samples in the future [210].

10. Summary and outlook

Mueller polarimetric imaging has demonstrated compelling potential for biomedical applications in recent years, as reviewed in this paper. The latest advances in this field include the investigation of the polarized light tissue interactions, the instrumentation of Mueller polarimeters, the interpretation of Mueller matrices and the development of Mueller polarimetric endoscopes and fibre sensors. The progress is paving the way to translate this technique into *in vivo* preclinical trials and for potential adoption into clinical practice for better tissue diagnosis and surgical guidance in the future. Many ongoing studies in this field are looking at further clinical applications, which can be combined with pathological inspections and statistical analysis to further translate physically meaningful data interpreted from the Mueller matrices into clinically meaningful data. The detection of optically thick tissues in a reflection mode would be more desirable and of more practical significance to apply the technique in surgery and optical biopsy than that in a transmission mode.

Mueller polarimetric imaging may sometimes contain redundant information for some tissue types, e.g. isotropically depolarizing tissues, non-birefringent tissues, for which partial Mueller polarimetry and Stokes polarimetry would be sufficient. It would be desirable to ensure that the most meaningful data are collected so as to fundamentally simplify the instrumentation and acquisition, and reduce the cost.

As a promising technique, Mueller polarimetric imaging for surgical and diagnostic applications is still in its infancy, and there is no doubt that much research still needs to be done. It is anticipated that Mueller polarimetric imaging can become an accessory imaging modality for surgical imaging in the future.

Reference

[1] V. V. Tuchin, V. Tuchin, Tissue optics: light scattering methods and instruments for medical diagnosis, SPIE press Bellingham, **2007**.

[2] D. Huang, E. A. Swanson, C. P. Lin, J. S. Schuman, W. G. Stinson, W. Chang, M. R. Hee, T. Flotte, K. Gregory, C. A. Puliafito *Science*. **1991**, 254, 1178-1181.

[3] A. K. Dunn, H. Bolay, M. A. Moskowitz, D. A. Boas *Journal of Cerebral Blood Flow & Metabolism*. **2001**, 21, 195-201.

[4] H. Cheng, Q. Luo, Q. Liu, Q. Lu, H. Gong, S. Zeng *Physics in Medicine and Biology*. **2004**, 49, 1347.

[5] S. Alali, A. Vitkin *J. Biomed. Opt.* **2015**, 20, 061104-061104.

[6] S. L. Jacques, J. C. Ramella-Roman, K. Lee *J. Biomed. Opt.* **2002**, 7, 329-340.

[7] S. L. Jacques, J. R. Roman, K. Lee *Lasers in Surgery and Medicine*. **2000**, 26, 119-129.

[8] W. Groner, J. W. Winkelman, A. G. Harris, C. Ince, G. J. Bouma, K. Messmer, R. G. Nadeau *Nat. Med.* **1999**, 5, 1209-1212.

[9] A. Da Silva, C. Deumié, I. Vanzetta *Biomed. Opt. Express*. **2012**, 3, 2907-2915.

[10] F. Snik, J. Craven-Jones, M. Escuti, S. Fineschi, D. Harrington, A. De Martino, D. Mawet, J. Riedi, J. S. Tyo in An overview of polarimetric sensing techniques and technology with applications to different research fields, Vol. (Ed.^Eds.: Editor), International Society for Optics and Photonics, City, **2014**, pp.90990B-90990B-90920.

[11] V. Backman, R. Gurjar, K. Badizadegan, I. Itzkan, R. R. Dasari, L. T. Perelman, M. S. Feld *Selected Topics in Quantum Electronics, IEEE Journal of*. **1999**, 5, 1019-1026.

[12] A. Pierangelo, A. Nazac, A. Benali, P. Validire, H. Cohen, T. Novikova, B. H. Ibrahim, S. Manhas, C. Fallet, M.-R. Antonelli, A.-D. Martino *Opt. Express*. **2013**, 21, 14120-14130.

[13] J. Chung, W. Jung, M. J. Hammer-Wilson, P. Wilder-Smith, Z. Chen *Appl. Opt.* **2007**, 46, 3038-3045.

[14] M.-R. Antonelli, A. Pierangelo, T. Novikova, P. Validire, A. Benali, B. Gayet, A. De Martino *Opt. Express*. **2010**, 18, 10200-10208.

[15] T. Novikova, A. Pierangelo, S. Manhas, A. Benali, P. Validire, B. Gayet, A. De Martino *Appl. Phys. Lett.* **2013**, 102, 241103.

[16] A. Pierangelo, A. Benali, M.-R. Antonelli, T. Novikova, P. Validire, B. Gayet, A. De Martino *Opt. Express*. **2011**, 19, 1582-1593.

[17] A. Pierangelo, S. Manhas, A. Benali, C. Fallet, M.-R. Antonelli, T. Novikova, B. Gayet, P. Validire, A. De Martino *J. Biomed. Opt.* **2012**, 17, 066009-066001.

[18] J. Rehbinder, S. Deby, H. Haddad, B. Teig, A. Nazac, A. Pierangelo, F. Moreau in *Diagnosis of uterine cervix cancer using Muller polarimetry: a comparison with histopathology, Vol. 9540* (Eds.: A. Amelink, I. A. Vitkin), Spie-Int Soc Optical Engineering, Bellingham, **2015**.

[19] P. Shukla, A. Pradhan *Opt. Express*. **2009**, 17, 1600-1609.

[20] A. Pierangelo, S. Manhas, A. Benali, C. Fallet, J.-L. Totobenazara, M.-R. Antonelli, T. Novikova, B. Gayet, A. De Martino, P. Validire *J. Biomed. Opt.* **2013**, 18, 046014-046014.

[21] S. Alali, K. J. Aitken, A. Schröder, A. Gribble, D. J. Bagli, I. A. Vitkin *Biomed. Opt. Express*. **2014**, 5, 621-629.

[22] A. Tata, A. Gribble, M. Ventura, M. Ganguly, E. Bluemke, H. J. Ginsberg, D. A. Jaffray, D. R. Ifa, A. Vitkin, A. Zarrine-Afsar *Chemical Science*. **2016**.

[23] P. G. Ellingsen, L. M. S. Aas, V. S. Hagen, R. Kumar, M. B. Lilledahl, M. Kildemo *J. Biomed. Opt.* **2014**, 19, 026002-026002.

[24] K. Brown. **2004**.

[25] R. A. Chipman *Handbook of optics*. **1995**, 2, 1-28.

[26] J. Li, G. Yao, L. V. Wang *J. Biomed. Opt.* **2002**, 7, 307-312.

[27] I. J. Vaughn, B. G. Hoover *Opt. Express*. **2008**, 16, 2091-2108.

[28] G. T. Georgiev, J. J. Butler in The effect of speckle on BRDF measurements, Vol. (Ed.^Eds.: Editor), International Society for Optics and Photonics, City, **2005**, pp.588203-588203-588212.

[29] A. Vitkin, N. Ghosh, A. d. Martino in *Tissue Polarimetry, Vol.*, John Wiley & Sons, Inc., **2015**, pp.239-321.

[30] D. Goldstein, D. H. Goldstein, Polarized Light, CRC Press, **2011**.

[31] S.-Y. Lu, R. A. Chipman *J. Opt. Soc. Am. A*. **1996**, 13, 1106-1113.

[32] R. A. Chipman in Polarization analysis of optical systems, Vol. (Ed.^Eds.: Editor), International Society for Optics and Photonics, City, **1988**, pp.10-31.

[33] R. A. Chipman *Appl. Opt.* **2005**, 44, 2490-2495.

[34] J. J. Gil, E. Bernabeu *Journal of Modern Optics*. **1986**, 33, 185-189.

[35] T.-T.-H. Pham, Y.-L. Lo *J. Biomed. Opt.* **2012**, 17, 0970021-09700215.

[36] J. J. Gil *Optics Communications*. **2016**, 368, 165-173.

[37] H. D. Noble, R. A. Chipman *Opt. Express*. **2012**, 20, 17-31.

[38] H. M. Shapiro, Practical flow cytometry, John Wiley & Sons, **2005**.

[39] J. R. Mourant, M. Canpolat, C. Brocker, O. Esponda-Ramos, T. M. Johnson, A. Matanock, K. Stetter, J. P. Freyer *J. Biomed. Opt.* **2000**, 5, 131.

[40] J. R. Mourant, J. P. Freyer, A. H. Hielscher, A. A. Eick, D. Shen, T. M. Johnson *Appl. Opt.* **1998**, 37, 3586-3593.

[41] S. L. Jacques *Physics in Medicine and Biology*. **2013**, 58, R37.

[42] L. V. Wang, H. Wu, Biomedical optics: principles and imaging, Wiley-Blackwell, **2007**.

[43] C. F. Boliren, D. R. Huffman *J Wiley & Sons, New York*. **1983**.

[44] H. C. Hulst, H. Van De Hulst, Light scattering by small particles, Courier Corporation, **1957**.

[45] B. T. Draine, P. J. Flatau *JOSA A*. **1994**, 11, 1491-1499.

[46] M. Xu, R. R. Alfano *Phys. Rev. Lett.* **2005**, 95, 213901.

[47] R. S. Gurjar, V. Backman, L. T. Perelman, I. Georgakoudi, K. Badizadegan, I. Itzkan, R. R. Dasari, M. S. Feld *Nat Med*. **2001**, 7, 1245-1248.

[48] R. S. Cotran, V. Kumar, T. Collins, S. L. Robbins. **1999**.

[49] S. G. Demos, R. R. Alfano *Appl. Opt.* **1997**, 36, 150-155.

[50] S. Demos, H. Radousky, R. Alfano *Opt. Express*. **2000**, 7, 23-28.

[51] N. T. Clancy, S. Arya, J. Qi, D. Stoyanov, G. B. Hanna, D. S. Elson *Biomed. Opt. Express*. **2014**, 5, 4108-4117.

[52] A. Pigula, N. T. Clancy, S. Arya, G. B. Hanna, D. S. Elson in Video-rate dual polarization multispectral endoscopic imaging, Vol. (Ed.^Eds.: Editor), International Society for Optics and Photonics, City, **2015**, pp.93330N-93330N-93334.

[53] J. Qi, C. Barrière, T. C. Wood, D. S. Elson *Biomed. Opt. Express*. **2012**, 3, 2087-2099.

[54] K. Kanamori *IPSJ Transactions on Computer Vision and Applications*. **2014**, 6, 34-38.

[55] K. Kanamori *J. Biomed. Opt.* **2015**, 21, 071105-071105.

[56] L. Perelman, V. Backman, M. Wallace, G. Zonios, R. Manoharan, A. Nusrat, S. Shields, M. Seiler, C. Lima, T. Hamano *Phys. Rev. Lett.* **1998**, 80, 627-630.

[57] R. Drezek, M. Guillaud, T. Collier, I. Boiko, A. Malpica, C. Macaulay, M. Follen, R. R. Richards-Kortum *J. Biomed. Opt.* **2003**, 8, 7-16.

[58] K. Sokolov, R. Drezek, K. Gossage, R. Richards-Kortum *Opt. Express*. **1999**, 5, 302-317.

[59] Y. Liu, Y. Kim, X. Li, V. Backman *Opt. Express*. **2005**, 13, 601-611.

[60] V. Backman, R. R. Dasari, R. Gurjar, I. Itzkan, L. Perelman, M. S. Feld in Polarized light scattering spectroscopy of tissue, Vol. (Ed.^Eds.: Editor), Google Patents, City, **2002**.

[61] Y. L. Kim, Y. Liu, R. K. Wali, H. K. Roy, M. J. Goldberg, A. K. Kromin, K. Chen, V. Backman *Selected Topics in Quantum Electronics, IEEE Journal of*. **2003**, 9, 243-256.

[62] Y. Liu, Y. L. Kim, V. Backman *Appl. Opt.* **2005**, 44, 2288-2299.

[63] A. Myakov, L. Nieman, L. Wicky, U. Utzinger, R. Richards-Kortum, K. Sokolov *J. Biomed. Opt.* **2002**, 7, 388-397.

[64] J. R. Mourant, T. M. Johnson, J. P. Freyer *Appl. Opt.* **2001**, 40, 5114-5123.

[65] L. T. Nieman, C.-W. Kan, A. Gillenwater, M. K. Markey, K. Sokolov *J. Biomed. Opt.* **2008**, 13, 024011-024011-024011.

[66] V. M. Turzhitsky, A. J. Gomes, Y. L. Kim, Y. Liu, A. Kromine, J. D. Rogers, M. Jameel, H. K. Roy, V. Backman *Appl. Opt.* **2008**, 47, 6046-6057.

[67] S. Ruderman, A. J. Gomes, V. Stoyneva, J. D. Rogers, A. J. Fought, B. D. Jovanovic, V. Backman *Biomed. Opt. Express*. **2010**, 1, 489-499.

[68] C. Kelley, S. Lakhani, D. Pickard, P. M. Ripley, I. J. Bigio, S. G. Bown, C. Saunders, G. Briggs, I. G. Rose *J. Biomed. Opt.* **2000**, 5, 221-228.

[69] I. J. Bigio, O. A'Amar, M. S. Hirsch in Elastic scattering spectroscopy for detection of prostate cancer: preliminary feasibility study, Vol. (Ed.^Eds.: Editor), International Society for Optics and Photonics, City, **2003**, pp.142-146.

[70] K. S. Johnson, D. W. Chicken, D. C. Pickard, A. C. Lee, M. Falzon, I. J. Bigio, M. R. Keshtgar, S. G. Bown, G. Briggs *J. Biomed. Opt.* **2004**, 9, 1122-1128.

[71] A. Dhar, K. S. Johnson, M. R. Novelli, S. G. Bown, I. J. Bigio, L. B. Lovat, S. L. Bloom *Gastrointestinal endoscopy*. **2006**, 63, 257-261.

[72] A. Sharwani, W. Jerjes, V. Salih, B. Swinson, I. Bigio, M. El-Maaytah, C. Hopper *Oral oncology*. **2006**, 42, 343-349.

[73] L. B. Lovat, K. Johnson, G. D. Mackenzie, B. R. Clark, M. R. Novelli, S. Davies, M. O'Donovan, C. Selvasekar, S. M. Thorpe, D. Pickard *Gut*. **2006**, 55, 1078-1083.

[74] Wallace*, Michael B, L. T. Perelman†, V. Backman†, J. M. Crawford §, M. Fitzmaurice // , M. Seiler¶, K. Badizadegan#, S. J. Shields*, I. Itzkan†, R. R. Dasari† *Gastroenterology*. **2000**, 119, 677-682.

[75] J. R. Mourant, T. J. Bocklage, T. M. Powers, H. M. Greene, M. H. Dorin, A. G. Waxman, M. M. Zsemlye, H. O. Smith *Journal of lower genital tract disease*. **2009**, 13, 216.

[76] J. R. Mourant, T. M. Powers, T. J. Bocklage, H. M. Greene, M. H. Dorin, A. G. Waxman, M. M. Zsemlye, H. O. Smith *Appl. Opt.* **2009**, 48, D26-D35.

[77] J. R. Mourant, O. C. Marina, C. K. Sanders in The Correlation between Side Scattering and Internal Structures of Mammalian Cells with and without Acetic Acid Exposure, Vol. (Ed.^Eds.: Editor), Optical Society of America, City, **2012**, pp.BW3B. 7.

[78] O. C. Marina, C. K. Sanders, J. R. Mourant *J. Biomed. Opt.* **2012**, 17, 085002-085002.

[79] O. Marina, A. Trujillo, C. Sanders, K. Burnett, J. P. Freyer, J. R. Mourant in The Effects of Acetic Acid on Mammalian Cells, Vol. (Ed.^Eds.: Editor), Optical Society of America, City, **2010**, pp.BSuD74.

[80] J. R. Mourant, O. C. Marina, H. O. Smith in In vivo Spectroscopy of Cervical Tissue, Vol. (Ed.^Eds.: Editor), Optical Society of America, City, **2012**, pp.JM3A.23.

[81] T. T. Wu, J. Y. Qu *Appl. Opt.* **2007**, 46, 4834-4842.

[82] T. Wu, T.-H. Cheung, J. Y. Qu, S.-F. Yim *J. Biomed. Opt.* **2010**, 15, 026001-026001-026007.

[83] L. Qiu, T. A. Larson, D. K. Smith, E. Vitkin, S. Zhang, M. D. Modell, I. Itzkan, E. B. Hanlon, B. A. Korgel, K. V. Sokolov *Selected Topics in Quantum Electronics, IEEE Journal of*. **2007**, 13, 1730-1738.

[84] C. S. Mulvey, A. L. Curtis, S. K. Singh, I. J. Bigio *Selected Topics in Quantum Electronics, IEEE Journal of*. **2007**, 13, 1663-1670.

[85] C. S. Mulvey, I. J. Bigio, C. A. Sherwood *J. Biomed. Opt.* **2009**, 14, 064013-064013-064014.

[86] C. S. Mulvey, K. Zhang, W. H. B. Liu, D. J. Waxman, I. J. Bigio *J. Biomed. Opt.* **2011**, 16, 117002.

[87] A. Kim, M. Moscoso *Physical Review E*. **2001**, 64, 026612.

[88] F. MacKintosh, J. Zhu, D. Pine, D. Weitz *Physical Review B*. **1989**, 40, 9342.

[89] C. M. Macdonald, S. L. Jacques, I. V. Meglinski *Physical Review E*. **2015**, 91, 033204.

[90] M. Xu, R. Alfano *Physical Review E*. **2005**, 72, 065601.

[91] D. Bicout, C. Brosseau, A. S. Martinez, J. M. Schmitt *Physical Review E*. **1994**, 49, 1767-1770.

[92] W. Cai, X. Ni, S. K. Gayen, R. R. Alfano *Physical Review E*. **2006**, 74, 056605.

[93] V. Sankaran, J. J. T. Walsh, D. J. Maitland *J. Biomed. Opt.* **2002**, 7, 300-306.

[94] J. Qi, M. Ye, M. Singh, N. T. Clancy, D. S. Elson *Biomed. Opt. Express*. **2013**, 4, 2433-2449.

[95] V. Sankaran, M. J. Everett, D. J. Maitland, J. T. Walsh *Opt. Lett.* **1999**, 24, 1044-1046.

[96] J. Beuthan, O. Minet, J. Helfmann, M. Herrig, G. Müller *Physics in Medicine and Biology*. **1996**, 41, 369.

[97] B. Kunnen, C. Macdonald, A. Doronin, S. Jacques, M. Eccles, I. Meglinski *Journal of Biophotonics*. **2015**, 8, 317-323.

[98] X. Feng, L. Sun, E. Zhang *Biomed. Opt. Express*. **2013**, 4, 958-966.

[99] I. A. Vitkin, R. C. N. Studinski *Optics Communications*. **2001**, 190, 37-43.

[100] S. Alali, M. Ahmad, A. Kim, N. Vurgun, M. F. G. Wood, I. A. Vitkin *J. Biomed. Opt.* **2012**, 17, 045004-045001.

[101] N. Ghosh, I. A. Vitkin *J. Biomed. Opt.* **2011**, 16, 110801.

[102] D. J. Maitland, J. T. Walsh *Lasers in Surgery and Medicine*. **1997**, 20, 310-318.

[103] L. V. Wang, G. L. Cote´, S. L. Jacques *J. Biomed. Opt.* **2002**, 7, 278-278.

[104] R. Kalluri, M. Zeisberg *Nature Reviews Cancer*. **2006**, 6, 392-401.

[105] P. Chen, M. Cescon, P. Bonaldo *Trends in Molecular Medicine*. **2013**, 19, 410-417.

[106] S. Alali, K. J. Aitken, A. Schröder, D. J. Bagli, I. A. Vitkin *J. Biomed. Opt.* **2012**, 17, 0860101-0860108.

[107] P. G. Ellingsen, M. B. Lilledahl, L. M. S. Aas, C. d. L. Davies, M. Kildemo *J. Biomed. Opt.* **2011**, 16, 116002-1160026.

[108] B. Cense, T. C. Chen, B. H. Park, M. C. Pierce, J. F. de Boer *Opt. Lett.* **2002**, 27, 1610-1612.

[109] B. Cense, T. C. Chen, B. H. Park, M. C. Pierce, J. F. De Boer *Investigative Ophthalmology & Visual Science*. **2004**, 45, 2606-2612.

[110] C. Ahlers, E. Götzinger, M. Pircher, I. Golbaz, F. Prager, C. Schütze, B. Baumann, C. K. Hitzenberger, U. Schmidt-Erfurth *Investigative Ophthalmology & Visual Science*. **2010**, 51, 2149.

[111] D. Côté, I. A. Vitkin *Opt. Express*. **2005**, 13, 148-163.

[112] D. Cote´, I. A. Vitkin *J. Biomed. Opt.* **2004**, 9, 213-220.

[113] N. Ghosh, M. F. G. Wood, S.-h. Li, R. D. Weisel, B. C. Wilson, R.-K. Li, I. A. Vitkin *Journal of Biophotonics*. **2009**, 2, 145-156.

[114] M. M. Engelgau, K. Narayan, W. H. Herman *Diabetes care*. **2000**, 23, 1563-1580.

[115] R. C. Weast, M. J. Astle, W. H. Beyer, CRC handbook of chemistry and physics, CRC press Boca Raton, FL, **1988**.

[116] R. Ossikovski, A. De Martino, S. Guyot *Opt. Lett.* **2007**, 32, 689-691.

[117] R. Ossikovski *JOSA A*. **2009**, 26, 1109-1118.

[118] N. Ortega-Quijano, J. L. Arce-Diego *Opt. Lett.* **2011**, 36, 1942-1944.

[119] R. Ossikovski *Opt. Lett.* **2011**, 36, 2330-2332.

[120] R. Ossikovski *Opt. Lett.* **2012**, 37, 220-222.

[121] O. Arteaga, B. Kahr *Opt. Lett.* **2013**, 38, 1134-1136.

[122] N. Ortega-Quijano, B. Haj-Ibrahim, E. García-Caurel, J. L. Arce-Diego, R. Ossikovski *Opt. Express*. **2012**, 20, 1151-1163.

[123] N. Agarwal, J. Yoon, E. Garcia-Caurel, T. Novikova, J.-C. Vanel, A. Pierangelo, A. Bykov, A. Popov, I. Meglinski, R. Ossikovski *Opt. Lett.* **2015**, 40, 5634-5637.

[124] H. D. Noble, S. C. McClain, R. A. Chipman *Appl. Opt.* **2012**, 51, 735-744.

[125] Z. Nan, J. Xiaoyu, G. Qiang, H. Yonghong, M. Hui *Appl. Opt.* **2009**, 48, 6734-6739.

[126] E. Du, H. He, N. Zeng, M. Sun, Y. Guo, J. Wu, S. Liu, H. Ma *J. Biomed. Opt.* **2014**, 19, 076013-076013.

[127] M. Sun, H. He, N. Zeng, E. Du, Y. Guo, C. Peng, Y. He, H. Ma *Appl. Opt.* **2014**, 53, 2949-2955.

[128] R. Liao, N. Zeng, X. Jiang, D. Li, T. Yun, Y. He, H. Ma *J. Biomed. Opt.* **2010**, 15, 036014-036014-036016.

[129] H. He, N. Zeng, E. Du, Y. Guo, D. Li, R. Liao, H. Ma *Photonics & Lasers in Medicine*. **2013**, 2, 129-137.

[130] H. He, N. Zeng, E. Du, Y. Guo, D. Li, R. Liao, Y. He, H. Ma *J. Biomed. Opt.* **2013**, 18, 046002-046002.

[131] H. He, M. Sun, N. Zeng, E. Du, S. Liu, Y. Guo, J. Wu, Y. He, H. Ma *J. Biomed. Opt.* **2014**, 19, 106007-106007.

[132] S. R. Cloude in Conditions For The Physical Realisability Of Matrix Operators In Polarimetry, Vol. 1166 (Ed.^Eds.: Editor), City, **1990**, pp.177-187.

[133] J. J. Gil, I. San José, R. Ossikovski *JOSA A*. **2013**, 30, 32-50.

[134] N. Ghosh, I. A. Vitkin, M. F. G. Wood *J. Biomed. Opt.* **2008**, 13, 044036-044036.

[135] N. Ghosh, M. F. Wood, I. A. Vitkin *J. Appl. Phys.* **2009**, 105, 102023.

[136] I. Ahmad, M. Ahmad, K. Khan, S. Ashraf, S. Ahmad, M. Ikram *J. Biomed. Opt.* **2015**, 20.

[137] J. Qi, D. S. Elson *Sci Rep*. **2016**, 6, 25953.

[138] R. Ossikovski, M. Anastasiadou, S. Ben Hatit, E. Garcia‐Caurel, A. De Martino *physica status solidi (a)*. **2008**, 205, 720-727.

[139] N. Ghosh, M. F. Wood, I. A. Vitkin *Optics Communications*. **2010**, 283, 1200-1208.

[140] R. Ossikovski, C. Fallet, A. Pierangelo, A. De Martino *Opt. Lett.* **2009**, 34, 974-976.

[141] R. Ossikovski, M. Foldyna, C. Fallet, A. De Martino *Opt. Lett.* **2009**, 34, 2426-2428.

[142] N. Ortega-Quijano, J. L. Arce-Diego *Opt. Express*. **2011**, 19, 14348-14353.

[143] S. Kumar, H. Purwar, R. Ossikovski, I. A. Vitkin, N. Ghosh *J. Biomed. Opt.* **2012**, 17, 105006-105006.

[144] M. Sun, H. He, N. Zeng, E. Du, Y. Guo, S. Liu, J. Wu, Y. He, H. Ma *Biomed. Opt. Express*. **2014**, 5, 4223-4234.

[145] M. F. G. Wood, N. Ghosh, M. A. Wallenburg, S.-H. Li, R. D. Weisel, B. C. Wilson, R.-K. Li, I. A. Vitkin *J. Biomed. Opt.* **2010**, 15, 047009-047009.

[146] A. Shuaib, X. Li, G. Yao *J. Biomed. Opt.* **2011**, 16, 025001-025001-025008.

[147] J. Soni, H. Purwar, H. Lakhotia, S. Chandel, C. Banerjee, U. Kumar, N. Ghosh *Opt. Express*. **2013**, 21, 15475-15489.

[148] G. C. Giakos, S. Marotta, C. Narayan, J. Petermann, S. Shrestha, J. Baluch, D. Pingili, D. B. Sheffer, L. Zhang, M. Zervakis, G. Livanos, M. Kounelakis *Measurement Science & Technology*. **2011**, 22.

[149] I. Ahmad, A. Gribble, M. Ikram, M. Pop, A. Vitkin *Journal of Biophotonics*. **2015**, n/a-n/a.

[150] H. He, N. Zeng, R. Liao, T. Yun, W. Li, Y. He, H. Ma *Opt. Express*. **2010**, 18, 15104-15112.

[151] P. Banerjee, J. Soni, H. Purwar, N. Ghosh, T. K. Sengupta *J. Biomed. Opt.* **2013**, 18, 035003-035003.

[152] J. S. Baba, J.-R. Chung, A. H. DeLaughter, B. D. Cameron, G. L. Cote´ *J. Biomed. Opt.* **2002**, 7, 341-349.

[153] M. H. Smith, P. D. Burke, A. Lompado, E. A. Tanner, L. W. Hillman in Mueller matrix imaging polarimetry in dermatology, Vol. 3911 (Ed.^Eds.: Editor), City, **2000**, pp.210-216.

[154] Y. A. Ushenko, O. V. Dubolazov, A. O. Karachevtsev *Optical Memory and Neural Networks*. **2011**, 20, 145-154.

[155] Y. A. Ushenko, A. Peresunko, B. Adel Baku *Advances in Optical Technologies*. **2010**, 2010.

[156] D. Li, H. He, N. Zeng, W. Xie, R. Liao, J. Wu, Y. He, H. Ma *Journal of Innovative Optical Health Sciences*. **2014**, 07, 1450009.

[157] X. Wang, J. Lai, Z. Li *Opt. Express*. **2012**, 20, 20771-20782.

[158] M. Ahmad, S. Ali, M. S. Mehmood, H. Ali, A. Khurshid, S. Firdous, S. Muhammad, M. Ikram *Appl. Spectrosc.* **2013**, 67, 1382-1389.

[159] W. Wang, L. G. Lim, S. Srivastava, J. Bok-Yan So, A. Shabbir, Q. Liu *Journal of Biophotonics*. **2015**, 9999, n/a-n/a.

[160] C. He, H. He, J. Chang, Y. Dong, S. Liu, N. Zeng, Y. He, H. Ma *Biomed. Opt. Express*. **2015**, 6, 2934-2945.

[161] Y. A. Ushenko *J. Biomed. Opt.* **2011**, 16, 066006-066006-066008.

[162] Y. A. Ushenko, M. I. Sidor, G. B. Bodnar, G. D. Koval *Quantum Electronics*. **2014**, 44, 785-790.

[163] N. Cuando-Espitia, F. Sanchez-Arevalo, J. Hernandez-Cordero *Biomed. Opt. Express*. **2015**, 6, 2953-2960.

[164] J. Chang, H. He, Y. Wang, Y. Huang, X. Li, C. He, R. Liao, N. Zeng, S. Liu, H. Ma *J. Biomed. Opt.* **2016**, 21, 056002-056002.

[165] Y. A. Ushenko *Opt. Spectrosc.* **2015**, 118, 1007-1016.

[166] J. Wang, W. Zheng, K. Lin, Z. Huang *Biomed. Opt. Express*. **2016**, 7, 1116-1126.

[167] J. Jagtap, S. Chandel, N. Das, J. Soni, S. Chatterjee, A. Pradhan, N. Ghosh *Opt. Lett.* **2014**, 39, 243-246.

[168] R. M. A. Azzam *Opt. Lett.* **1978**, 2, 148-150.

[169] R. M. A. Azzam, A. G. Lopez *J. Opt. Soc. Am. A*. **1989**, 6, 1513-1521.

[170] R. M. A. Azzam, E. Masetti, I. M. Elminyawi, F. G. Grosz *Rev. Sci. Instrum.* **1988**, 59, 84-88.

[171] M. Dubreuil, S. Rivet, B. Le Jeune, J. Cariou *Opt. Express*. **2007**, 15, 13660-13668.

[172] N. Hagen, K. Oka, E. L. Dereniak *Opt. Lett.* **2007**, 32, 2100-2102.

[173] K. Oka, T. Kato *Opt. Lett.* **1999**, 24, 1475-1477.

[174] S. Alali, T. Yang, I. A. Vitkin *Opt. Lett.* **2013**, 38, 2997-3000.

[175] S. Alali, A. Gribble, I. A. Vitkin *Opt. Lett.* **2016**, 41, 1038-1041.

[176] R. M. A. Azzam *Opt. Lett.* **1985**, 10, 309-311.

[177] J. L. Pezzaniti, D. B. Chenault in A division of aperture MWIR imaging polarimeter, Vol. (Ed.^Eds.: Editor), International Society for Optics and Photonics, City, **2005**, pp.58880V-58880V-58812.

[178] G. P. Nordin, J. T. Meier, P. C. Deguzman, M. W. Jones *J. Opt. Soc. Am. A*. **1999**, 16, 1168-1174.

[179] W.-L. Hsu, G. Myhre, K. Balakrishnan, N. Brock, M. Ibn-Elhaj, S. Pau *Opt. Express*. **2014**, 22, 3063-3074.

[180] X. Zhao, A. Bermak, F. Boussaid, V. G. Chigrinov *Opt. Express*. **2010**, 18, 17776-17787.

[181] J. S. Tyo, D. L. Goldstein, D. B. Chenault, J. A. Shaw *Appl. Opt.* **2006**, 45, 5453-5469.

[182] A. De Martino, E. Garcia-Caurel, B. Laude, B. Drévillon *Thin Solid Films*. **2004**, 455, 112-119.

[183] A. Ambirajan, J. D. C. Look in Optimum angles for a Mueller matrix polarimeter, Vol. 2265 (Ed.^Eds.: Editor), City, **1994**, pp.314-326.

[184] R. A. Horn, C. R. Johnson, Matrix analysis, Cambridge university press, **2012**.

[185] D. S. Sabatke, A. M. Locke, M. R. Descour, W. C. Sweatt, J. P. Garcia, E. L. Dereniak, S. A. Kemme, G. S. Phipps in Figures of merit for complete Stokes polarimeter optimization, Vol. (Ed.^Eds.: Editor), International Society for Optics and Photonics, City, **2000**, pp.75-81.

[186] R. Azzam, A. G. Lopez *JOSA A*. **1989**, 6, 1513-1521.

[187] R. Azzam, E. Masetti, I. Elminyawi, F. Grosz *Rev. Sci. Instrum.* **1988**, 59, 84-88.

[188] E. Compain, S. Poirier, B. Drevillon *Appl. Opt.* **1999**, 38, 3490-3502.

[189] C. Macias-Romero, P. Török *Journal of the European Optical Society-Rapid publications*. **2012**, 7.

[190] J. Wolfe, R. A. Chipman *Opt. Express*. **2004**, 12, 3443-3451.

[191] R. A. Chipman *Optical engineering*. **1989**, 28, 280290-280290-.

[192] J. P. McGuire, R. A. Chipman *Appl. Opt.* **1994**, 33, 5080-5100.

[193] J. P. McGuire, R. A. Chipman *Appl. Opt.* **1994**, 33, 5101-5107.

[194] R. M. A. Azzam, M. M. K. Howlader *Opt. Lett.* **2001**, 26, 1607-1608.

[195] X. Xu, W. Huang, M. Xu *Opt. Express*. **2015**, 23, 27911-27919.

[196] T. C. Wood, D. S. Elson *Biomed. Opt. Express*. **2010**, 1, 463-470.

[197] J. Qi *PhD thesis*. **2014**.

[198] J. Chang, N. Zeng, H. He, Y. Guo, H. Ma *J. Biomed. Opt.* **2014**, 19, 095001-095001.

[199] R. Liang, Optical design for biomedical imaging, Spie Press, **2010**.

[200] J. Chang, N. Zeng, H. He, Y. He, H. Ma *Opt. Lett.* **2014**, 39, 2656-2659.

[201] J. Chang, H. He, C. He, Y. Wang, N. Zeng, R. Liao, H. Ma *Appl. Opt.* **2015**, 54, 7424-7432.

[202] S. C. Rashleigh, R. Ulrich *Opt. Lett.* **1978**, 3, 60-62.

[203] E. Collett, Polarized light in fiber optics, SPIE Press, **2003**.

[204] M. K. Swami, S. Manhas, P. Buddhiwant, N. Ghosh, A. Uppal, P. K. Gupta *Opt. Express*. **2006**, 14, 9324-9337.

[205] Y. Wang, Y. Guo, N. Zeng, D. Chen, H. He, H. Ma *J. Biomed. Opt.* **2015**, 20, 065003-065003.

[206] J. Qi, M. Singh, N. Clancy, D. S. Elson in Mueller Polarimetric Endoscopy, Vol. (Ed.^Eds.: Editor), Optical Society of America, City, **2014**, pp.AM2O.1.

[207] R. Jain, R. Kasturi, B. G. Schunck, Machine vision, McGraw-Hill New York, **1995**.

[208] M. Murakumo, T. Ushiki, K. Abe, K. Matsumura, Y. Shinno, T. Koyanagi *The Journal of Urology*. **1995**, 154, 251-256.

[209] S. Manhas, J. Vizet, S. Deby, J.-C. Vanel, P. Boito, M. Verdier, A. De Martino, D. Pagnoux *Opt. Express*. **2015**, 23, 3047-3054.

[210] S. Rivet, A. Bradu, A. Podoleanu *Opt. Express*. **2015**, 23, 23768-23786.